# 1

# Introduction to Capillarity and Wetting Phenomena



The goal of electrowetting (EW) is to manipulate small amounts of liquid on solid surfaces by tuning the wettability using electric fields. Many phenomena encountered in EW experiments are actually not special to *electro* wetting and *electro* capillarity. They are simply wetting and capillary phenomena that can be observed in many circumstances with surfaces of more or less complex geometry and more or less complex distributions of wettability. EW is rather unique in its ability to change contact angles over a very wide range in a very fast and usually very reproducible manner. Therefore, EW has enabled an unprecedented degree of control of drop shapes and dynamics – and along with it a plethora of possible applications. Nevertheless, many basic observations in EW are still variants of classical wetting and capillary phenomena and hence subject to the general laws of capillarity. To understand the phenomena that we encounter in EW experiments and to be able to fully exploit the potential of EW technology, we therefore need a good grasp of the physical principles of wetting and capillarity. The purpose of this first chapter is to introduce the reader to these basic concepts. We will discuss in Section 1.1 the microscopic origin of surface tension and interfacial energies starting from molecular interaction forces. In Sections 1.2 and 1.3, we introduce the two basic laws governing the mechanical equilibrium of liquid microstructures, the Young–Laplace law and the Young–Dupré equation. In Section 1.4, gravity is added as an additional external body force. Section 1.5 is devoted to a concise but somewhat formal mathematical derivation of the fundamental equations that were discussed in Sections 1.2–1.4. Less mathematically interested readers can skip that section without missing important physical results. In Section 1.6, we address aspects of wetting on the nanoscale and introduce concepts such as the disjoining pressure and the effective interface potential that are relevant, among others, in the vicinity of the three-phase contact line and for the stability of nanometric films. In Section 1.7, we discuss some consequences of surface heterogeneity such as contact angle hysteresis and superhydrophobicity. In order to provide the reader with an intuitive understanding of the theoretical concepts and formulas, we will discuss a variety of classical capillary phenomena frequently switching between force balance arguments and considerations based on energy minimization.

A deeper discussion of many aspects addressed here can be found in the excellent textbook by deGennes et al. [1] that we will refer to multiple times.

*Electrowetting: Fundamental Principles and Practical Applications,*
First Edition. Frieder Mugele and Jason Heikenfeld.

## 1.1 Surface Tension and Surface Free Energy

Capillary and wetting phenomena are important on small scales. Small scales always imply large surface-to-volume ratios: the smaller the system, the larger the fraction of atoms or molecules that is located at interfaces. This is *the* fundamental reason why interfacial effects are crucial in all branches of micro- and nanotechnology, including micro- and nanofluidics. Being *at* the surface means being within the range of molecular interaction forces of the geometric interface. Using a typical value of, say, $\Delta r = 1$ nm we can simply estimate the fraction of molecules in a small drop that is affected by the interface: The volume of a drop or radius $r$ is $V = 4\pi r^3/3$. The volume of a shell of thickness $\Delta r$ is $V_s = 4\pi r^2 \Delta r$. Hence the ratio is $\Delta V_s/V = \Delta r/3r$. For a millimeter-sized drop, one molecule in three million is thus *at* the surface. For a micrometer-sized drop, the ratio is one in three thousand. These surface molecules, not the ones inside the bulk of the drop, determine the equilibrium shape of the drop.

### 1.1.1 The Microscopic Origin of Surface Energies

Throughout this book, we will consider liquids as continuous media characterized by material properties such as density, viscosity, and cohesive energy. Interfaces between two different phases such as liquid and vapor or liquid and solid are characterized by an interfacial energy or tension $\gamma$. For the specific interface between a liquid and its own vapor, it is common to speak of surface energy or surface tension. Both expressions, interfacial energies and tensions, mean the same thing, and we will use them interchangeably throughout this book. A surface energy is an excess free energy per unit area of the surface. It is measured in Joule per square meter or more frequently in milli Joule per square meter because the latter turns out to be more convenient for most common liquids. A surface tension is a tensile force per unit length acting along the surface. It is measured in Newton per meter, or in milli Newton per meter, which is dimensionally equivalent an energy per unit area. (In older books, you will sometimes find surface tensions reported in dyn/cm, which is numerically equivalent to mN/m.) These two complementary perspectives have their origin in complementary experimental observations and conceptual approaches. As often in mechanics, a given problem can be considered either from the perspective of energy minimization or from the perspective of force balance. Both views are perfectly equivalent. As classical theoretical mechanics tells us, Newton's equations of motion are the differential equations that any solution of a mechanical problem has to fulfill in order to minimize the Lagrangian and thus, in equilibrium, the energy of the system. Whether energy minimization or force balance is more convenient or more intuitive to solve a specific problem depends on the problem at hand – and to some extent on personal taste.

Why is there an excess energy associated with an interface? To understand this point, it is convenient to deviate for once from our general continuum picture and to instead consider the individual molecules and their mutual interaction. Let us first look at a reference molecule somewhere in the bulk of the liquid drawn

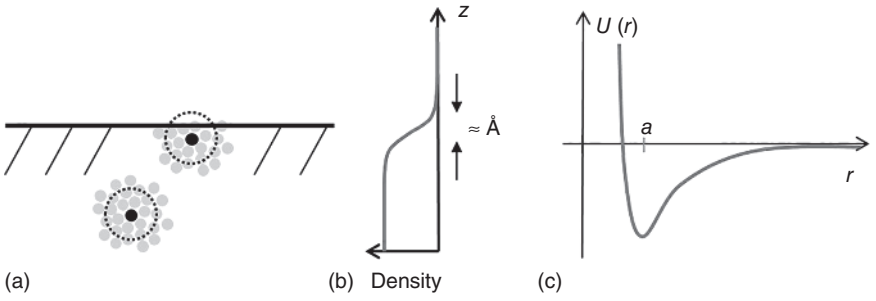


**Figure 1.1** (a) Schematic illustration of one specific molecule (black) in the bulk liquid interacting with neighbors (gray) within the range of interactions of the molecular forces (dotted circle) and a second molecule close to the interface that is missing binding partners on the opposite side. (b) Density profile at the liquid surface with a gradual transition from the bulk liquid density to the vapor density. (c) Typical molecular interaction potential between two molecules with a minimum close to the molecular diameter *a*.

in black in the bottom of Figure 1.1a. The reference molecule interacts with its neighbors via some molecular interaction potential. The details of this potential are characteristic for each specific liquid. While all relevant molecular interactions are fundamentally electromagnetic in nature, there are different flavors such as direct Coulomb interactions between charged ions, charge–dipole interactions, dipole–dipole interaction, van der Waals interaction, etc. A detailed discussion can be found in classical textbooks of surface forces, such as the ones by Butt and Kappl [2] and by Israelachvili [3]. Notwithstanding all the details, the generic shape of the interaction potentials usually looks as sketched in Figure 1.1c. There is a strong repulsive barrier at short distances that prevents the molecules from overlapping, and there is an attractive force with a range of typically a few molecular diameters that depends on the specific interaction. The minimum of the potential determines the average separation of the molecules and thus the density of the fluid. In practice liquids are very dense, and molecules continuously bounce into the repulsive potential barrier. The target molecule interacts with all its neighbors (drawn in gray) within the range of the interaction potential, as indicated by the dashed circle in Figure 1.1a. The sum of the interaction energy with all the neighbors within this range determines the cohesive energy $E_{coh}$ of the liquid. This is the reference energy of a molecule in the bulk. If we now consider a second molecule close to the surface, it is obvious that that molecule lacks binding partners above the liquid surface. As a consequence, it has less binding energy than the reference molecule in the bulk. This lack of binding energy constitutes an excess energy as compared with the reference state. If we denote the area per molecule at the interface as $a^2$, we obtain an estimate for the surface energy based on a very generic atomistic picture:

$$\gamma \approx \frac{E_{coh}}{2a^2} \tag{1.1}$$

We thus expect the surface tension to scale with cohesive energy of the liquid. Table 1.1 gives an overview of the surfaces tensions as well as other properties of liquids commonly used in EW. Generally, more polar molecules (stronger dipole,

**Table 1.1** Physical properties of some common liquids.

| | Surface tension ($mJ\,m^{-2}$) | Boiling temperature (°C) | Density ($kg\,m^{-3}$) | Viscosity (mPa s) | Vapor pressure (kPa) |
|---|---|---|---|---|---|
| Water (25 °C) | 72 | 100 | 997 | 0.89 | |
| Water (100 °C) | 58 | 100 | 972 | 0.354 (80°) | 100 |
| Ethanol | 22 | 78 | 789 | 1.074 | 6.1 |
| Hexanol | 25.7 | 158 | 814 | | 0.1 |
| Hexane | 18.4 | 68 | 655 | 0.29 | 17.6 |
| Decane | 23.8 | 174 | 730 | 0.92 | 0.195 |
| Hexadecane | 27.5 | 287 | 770 | 0 | $< 0.01$ |
| Glycerol | 64 | 290* | 1260 | | $< 10^{-4}$ |
| Ethylene glycol | 47.7 | 197 | 1110 | | 0.005 |
| Silicone oil (MW 100–100 000) | $\approx 20$ | | $\approx 900$ | $1–10^{6}$ | $1–10^{-4}$ |
| Mercury | 485 | 357 | 13 540 | | $<2 \times 10^{-4}$ |

stronger Coulomb forces) exhibit stronger attractive forces. Hence, they typically display a higher cohesive energy, higher boiling point, and higher surface tension. Water with its very large dipole moment is an example of a liquid with a particularly high cohesive energy in view of its low molecular weight. Even stronger cohesive forces are found for liquid metals, for which the cohesion is caused metallic bonds and thus by delocalized electrons.

Our atomistic picture and the estimate of the surface energy are obviously rather rough. Nevertheless, it illustrates a number of important points. For instance, we see from the finite range of the molecular interaction forces that the surface tension is not *located* strictly at the surface. Rather, it arises within the first few layers of molecules at the interface. More rigorous theories for calculating surface tensions in liquid state theory include such effects (see, e.g. [4]).

Another aspect worth noting is that the molecules in a liquid are obviously in vigorous permanent thermal motion. Molecular neighbors change on a picosecond time scale in conventional fluids. What matters for the surface tension is the average interaction energy, which is nevertheless a well-defined sharp value because it reflects an average over macroscopic numbers of molecules and molecular collision events. The relevant type of energy under such conditions is a *free* energy. It includes the effect of random thermal motion in the form of entropy. Surface tensions are excess *free* energies – not pure binding energies as our simplistic picture suggested. For a liquid surface, thermally activated capillary waves carry the entropy similar to phonons in a crystal. The amplitude of these waves is very small, typically not more than a molecular diameter. Yet, the population and amplitude of these capillary waves increase with increasing temperature. As a consequence, surface energies of liquids typically decrease with a temperature coefficient of the order of $-0.1\,mJ\,m^{-2}\,K^{-1}$. For water, this means that the surface tension decreases from $73\,mJ\,m^{-2}$ at 25 °C to $58\,mJ\,m^{-2}$ at 100 °C.

Another consequence of the thermal agitation and the discreteness of the molecules is that the position of the liquid surface is not perfectly sharp. Rather than decreasing abruptly from the liquid density to the vapor density, the interface is characterized by a transition that is smeared out over a small but finite region, as sketched in Figure 1.1b. Except for the vicinity of a critical point, the width of this transition region is of the order of one molecular diameter. Nevertheless, this gradual decrease of the density provides us with an intuitive way of understanding that surface energies act as tensions, i.e. as tensile forces tangential to the surface: In the bulk, the average distance between the molecules is given by the minimum of the interaction potential $U(r)$ (see Figure 1.1c). As mentioned above, this distance determines the density of the bulk liquid. Within the transition zone from liquid to vapor, the average distance between adjacent molecules gradually increases. For intermolecular separations slightly larger than $a$ in Figure 1.1c but still within the range of the potential, adjacent molecules experience net attractive forces. Averaged over the interfacial layer, this leads to a net tensile force within the range of the density gradient. This force tries to reduce the surface area like the tension of a rubber balloon.

So far, we have only been talking about surface tensions, i.e. about the interface between liquid and vapor. Our reasoning can be easily extended to estimate the interfacial energy of liquid–liquid interfaces. Assume that the vapor phase on the top of the surface in Figure 1.1a is replaced by a second fluid phase. Within the range of the molecular interaction potential, molecules of liquid A, lack binding partners of the same species on the opposite side of the interface. The same applies vice versa to the B molecules on other side of the interface. The fact that the liquid A and B don't mix implies that A and B molecules are each more strongly attracted to their own species than to the other one. As a consequence, the presence of the interface gives rise to an excess energy, i.e. a positive interfacial tension $\gamma_{AB}$. Now, what happens if A and B molecules attract each other more strongly than A molecules and B molecules among themselves? In this case, the presence of an A–B interface would actually reduce the free energy of the system, i.e. the A–B interfacial energy would be negative. As a consequence, the system gains energy by increasing the interfacial area; it spontaneously emulsifies and eventually mixes on molecular scales. Such systems exist. Yet, they do not form two thermodynamically stable separate phases.

In a similar manner, we can extend the concept of interfacial energy to interfaces between solids and liquids and solids and vapor. We will denote the corresponding interfacial tensions by $\gamma_{sl}$ and $\gamma_{sv}$, respectively. For liquid–vapor surface tensions, we drop the subscript for simplicity and simply write the symbol $\gamma$. For the remainder of this book, we will return to the continuum picture, and we will consider interfaces between adjacent phases as perfectly sharp.

### 1.1.2 Macroscopic Definition of Surface Energy and Surface Tension

Thermodynamically, the macroscopic surface energy is defined as the amount of mechanical work $\delta W$ required to deform a given amount of liquid in such a way

that the total surface area changes by $dA$:

$$\delta W = \gamma dA \tag{1.2}$$

Given our microscopic picture of surface energy, this definition makes perfect sense. All the molecules at the surface have an excess energy compared with ones in the bulk. Creating more surface area while keeping the number of molecules (and the density) constant implies transferring molecules from the bulk to the surface. Hence, we need to perform work against the molecular interaction forces. That mechanical work is stored as additional surface energy in the total Gibbs free energy $G$ of the system. Thus we can also write

$$\gamma = \left.\frac{\partial G}{\partial A}\right|_{N,P,T} \tag{1.3}$$

The existence of a finite macroscopic surface tension $\gamma$ also explains why drops assume a spherical shape in the absence of gravity or other external forces: Drops are free to adjust their shape in order to minimize their energy. Hence, they adapt their shape such that the surface area is minimal while keeping the volume constant. Since a sphere is the geometric object with the smallest surface-to-volume ratio, it is the equilibrium shape of free drops. Obviously, this is only true for free drops. As soon as the drop is subjected to external forces or to boundary conditions, e.g. due to contact with a solid surface, the equilibrium shape is in general no longer spherical.

The macroscopic definition of surface tension as a mechanical force per unit length is perhaps even more intuitive. Unlike the mechanical work required to deform a drop, the tensile forces exerted by liquid surfaces on solid objects can be visualized and measured very easily: Consider a U-shaped solid frame, made, for instance, of an open-bent paper clip, as sketched in Figure 1.2a. We place a straw across the two legs to close the U and span a soap film between the three sides of the U and the straw. As soon as we release the straw, it gets pulled toward the left by the soap membrane (see Figure 1.2). Not surprisingly, the force that pulls the straw is proportional to the length $l$ of the straw. Except for this geometric factor, the force is determined by the properties of the liquid, i.e. in this case the soap membrane. The coefficient relating the force $F$ to the length $l$ of the straw is the macroscopic surface tension:

$$F = 2\gamma l \tag{1.4}$$

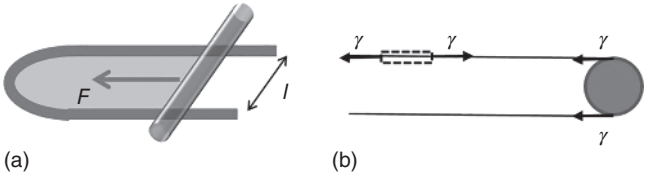


**Figure 1.2** (a) Schematic of a rod placed perpendicular across a U-shaped object is pulled toward the left by the surface tension of a thin soap membrane (gray). (b) Zoomed view of the top and bottom surface of the soap membrane and the tensile interfacial tension forces acting on a control volume (dashed) within the interfaces and on the solid boundary holding the membrane.

The factor 2 in the equation accounts for the two liquid surfaces on the top and bottom side of the soap membrane. Both pull on the straw with the same force. Again, we can relate the macroscopic thermodynamic definition to our atomistic picture of the surface tension: Tensile forces are present everywhere within the liquid surface. For an arbitrary element of the surface, tensile forces pulling from different directions balance each other, as sketched in Figure 1.2b. Wherever the liquid surface merges into a solid border of our U-shaped paper clip or into the straw, these tensile stresses must be balanced by the solid surface according to Newton's third law. The U-shaped paper clip becomes slightly deformed, and the mobile straw accelerates. In fact, the measurement of mechanical forces acting on solid objects is one of the most direct and widely spread methods to determine the surface tension of liquids. Tensile forces due to surface tension form an important part of capillary forces that hold sandcastles together or stick our wet hair together into bundles.

## 1.2 Young–Laplace Equation: The Basic Law of Capillarity

### 1.2.1 Laplace's Equation and the Pressure Jump Across Liquid Surfaces

As already mentioned, the existence of surface tension has profound consequences for the equilibrium shape of liquid structures. One of the most basic consequences is the existence of a pressure jump across curved liquid surfaces (and liquid–liquid interfaces). The origin of this pressure jump can be illustrated by considering a drop that is connected via a thin needle to a reservoir with a piston, as shown in Figure 1.3. If we move the piston forward and push liquid from the reservoir into the drop, we increase the surface area of the drop. If the drop radius is increased by $dr$, the surface area has increased by $dA = 8\pi R\, dR$.

Consequently, we have increased the Gibbs free energy of the drop by increasing its surface energy by $dG = \gamma\, dA$. To achieve this increase in surface energy, mechanical work $dW = F\, dx$ has to be performed to move the piston. Since the force on the piston is product of the area $A_p$ of the piston times the difference between the ambient pressure $P_0$ on the left and the drop pressure $P_{drop}$ on the right (see Figure 1.3), we can equate $dW = (P_{drop} - P_0)A_p dx = \Delta P_L dV$. Equating mechanical work and increase in surface energy, we find

$$\Delta P_L = \gamma \frac{dA}{dV} = \frac{2\gamma}{R} \tag{1.5}$$

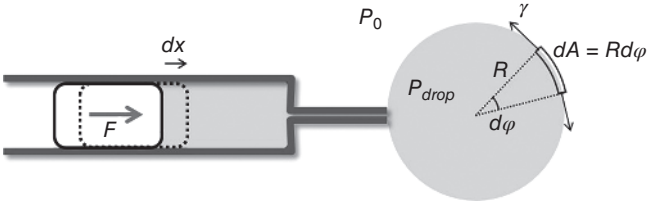


**Figure 1.3** Illustration of the derivation of Laplace pressure.

For the right-hand part of the equation, we made explicit use of the spherical shape of the drop by inserting $dV = 4\pi R^2 dR$. The pressure inside the drop thus exceeds the pressure in the ambient atmosphere by an amount that is given by the surface tension times $2/R = 2\kappa$. $\kappa = 1/R$ is called the (mean) curvature of the surface. (We will see below why the expression *mean* curvature makes sense.) This excess pressure, which is a direct consequence of the existence of surface tension, is generally known as Laplace pressure, paying tribute to the French mathematician and physicist Pierre-Simon Laplace, who studied this phenomenon in the early nineteenth century. In parallel Thomas Young studied the same phenomenon in England. Equation (1.5) and its generalized version that we will discuss below are therefore known as Young–Laplace equation.

In addition to the energy picture, it is instructive to consider the same problem from the perspective of force balance. We consider a little volume element $dV = dR\, dA$ that is enclosed by area elements $dA$ just inside and just outside the liquid surface spaced by a radial distance $dR$, as shown in Figure 1.3. The forces acting on this volume element consist of the surface tension force that pulls tangentially along the surface and the pressure forces on the inside and on the outside of the liquid. The components along the $\phi$-directions cancel for symmetry reasons as in the case of the flat surface considered in Figure 1.2b. Due to the finite curvature of the drop, however, there is also a net surface tension force $d\vec{f}_\gamma = -\gamma\, d\varphi\, \vec{e}_r$ oriented radially inward. (For simplicity, we consider the system as two-dimensional.) The pressure $P_{drop}$ on the liquid side is acting along the arc $Rd\phi$ and results in a net force pushing radially outward. Similarly, the ambient pressure $P_0$ leads to an inward-oriented force, leading together to a net pressure force $d\vec{f}_p = (P_{drop} - P_0)\, Rd\phi\, \vec{e}_r$. Balancing pressure and surface tension forces, we recover Eq. (1.5). It is important to note that the resulting excess pressure $\Delta P_L = P_{drop} - P_0$ in the fluid is a regular isotropic pressure that is felt everywhere inside the fluid notwithstanding the fact that it arises from the directional surface tension forces, which act along the interface.

The Laplace pressure inside a drop can become quite considerable for small drops. As a rule of thumb, it is useful to remember that a water drop with a radius of 1 µm has a Laplace pressure of approximately 1 bar – as much as the hydrostatic pressure due to a water column with a height of 10 m. For even smaller drops, as they are frequently produced and handled in nanofluidic devices, Laplace pressures become even higher.

The form of the Young–Laplace equation that we wrote down in Eq. (1.5) is actually only a special form for spherical drops of the full Young–Laplace equation. In general, liquids can assume more complex nonspherical shapes depending on the boundary conditions that we impose. Figure 1.4a shows a drop squeezed between two solid cylinders at two different distances. Obviously, a single radius of curvature is not sufficient to characterize such three-dimensional surfaces. In such cases, liquid surfaces are described by two different radii of curvature, $R_1$ and $R_2$. At any given point on the surface, $R_1$ and $R_2$ are defined by intersecting the liquid surface with two perpendicular planes, both containing

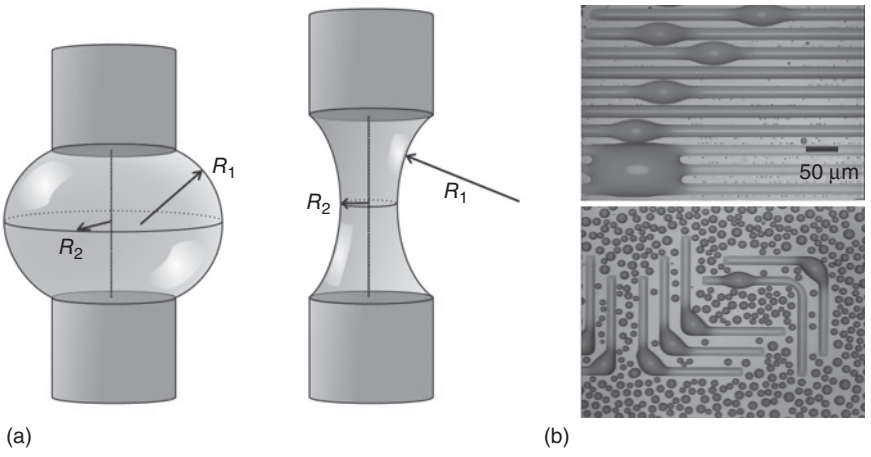


**Figure 1.4** Complex three-dimensional liquid microstructures. (a) Schematic of a liquid drop squeezed between two solid cylinders at variable distance showing the two perpendicular radii of curvature. (b) Microstructures of water condensed onto parallel (top) and elbow-shaped (bottom) hydrophilic stripes on an otherwise hydrophobic surface. Source: Adapted from Ref. [5]. See also Ref. [6].

the local surface normal. The resulting values of $R_1$ and $R_2$ will in general depend on the azimuthal orientation of the two surfaces. As we rotate the two surfaces around the surface normal, there will be a unique orientation, for which $R_1$ and $R_2$ assume a maximum and a minimum value, respectively. These maximum and minimum values are known as *principal* radii of curvature. The *mean curvature*, the specific combination $\kappa = (1/R_1 + 1/R_2)/2$, *is* a well-defined quantity, which determines the pressure jump across the liquid surface. With these definitions, the general version of the Young–Laplace law reads

$$\Delta P_L = 2\gamma\kappa \tag{1.6}$$

In this generalized version, the Young–Laplace law has somewhat deeper implications than discussed so far. Of course, it still provides the local value of the pressure jump upon crossing a liquid surface of curvature $\kappa$. But in addition, the law also states that $\kappa$ is constant everywhere along any connected liquid structure in mechanical equilibrium in the absence of other external forces. No matter how complex it may look, every equilibrated liquid surface is a surface of constant mean curvature. Any position dependence of $\kappa$ along the surface would imply pressure gradients within the fluid that would immediately set the fluid in motion. The resulting fluid flow would continue until all initial pressure gradients are balanced in a final state of constant mean curvature.

A few more comments are in order: First, for a sphere, $R_1$ and $R_2$ are obviously both equal and independent of the position by symmetry. In this case, the expression for the mean curvature reduces to $\kappa = 1/R$, as already stated above, and the full Young–Laplace equation reduces to its simplified form, Eq. (1.5).

Another important limiting case is the situation $R_1, R_2 \to \infty$. This corresponds to a flat surface. In this case, the pressures in the liquid phase and in the ambient phase are identical, i.e. $\Delta P_L = 0$. Second, looking at the right-hand side (RHS) of Figure 1.4a, we notice that the center of the local circle of curvature can be either inside ($R_2$) the liquid or outside ($R_1$). The former corresponds to the situation of a sphere. It gives rise to a positive excess pressure inside the drop, and hence we assign the positive sign to $R_2$ under these conditions. The latter corresponds to a negative radius of curvature $R_1$ and hence gives rise to a reduction of the pressure inside the liquid as compared with the ambient phase. For liquid drops in ambient vapor, the sign convention is thus straightforward: A radius of curvature is counted positive if the center of the circle is inside the liquid phase and it is counted negative in the opposite case. If we only know it is a mathematical function $h(x, y)$ describing the shape of an interface, it is not a priori clear what is *inside* and *outside*. It is therefore always very important to verify that the sign of the pressure drop in any calculation is in accordance with the physical problem at hand. For two immiscible liquids such as oil and water, the situation is in fact ambiguous, and $\Delta P_L$ may either be defined as $P_{water} - P_{oil}$ or vice versa.

As a mathematical expression, Eq. (1.6) does not look very complicated. Yet, this changes as soon as we write down an explicit expression for the radii of curvature in a specific coordinate system. Frequently, it is convenient to parameterize the shape of a liquid surface as a function $h(x, y)$ that specifies the local position of the interface above some reference plane. In this case, the explicit expression reads

$$\Delta P_L = 2\gamma\,\kappa = \gamma\,\frac{\partial_{xx}h(1+(\partial_y h)^2) - 2\partial_x h\,\partial_y h\,\partial_{xy}h + \partial_{yy}h(1+(\partial_x h)^2)}{(1+(\partial_x h)^2+(\partial_y h)^2)^{3/2}} \tag{1.7}$$

This equation reveals that the Young–Laplace law is in fact a nonlinear second-order partial differential equation for the surface $h(x, y)$. Such equations are difficult to solve and require in most cases a numerical approach. Given this complex structure of the governing equation, it is also not surprising that problems in capillary often lead to counterintuitive surface geometries.

Analytical solutions of the Young–Laplace equation usually only exist in case of specific symmetries or otherwise simplifying conditions. A common simplification that applies in many problems of thin film flows is the small slope approximation. In this case, the gradients of the surface are small, i.e. $|\,\partial_x h\,|, |\,\partial_y h\,| \ll 1$. As a consequence, we can neglect all the (quadratic) terms involving gradients of $h$. Equation (1.7) then reduces to

$$\Delta P_L = 2\gamma\,\kappa(x,y) = \gamma\,\nabla^2 h(x,y) \tag{1.8}$$

where $\nabla^2 = \partial_{xx} + \partial_{yy}$ is the Laplace operator in two dimensions. This equation is linear and hence much simpler to treat. Being a linear equation, any superposition of two solutions will also be a solution of the underlying equation, allowing for a convenient decomposition of the surface profile in Fourier modes.

Another common situation in applications is cylindrically symmetric problems, such as the one of the capillary bridges in Figure 1.4a. In this case, the Young–Laplace equation is best considered in cylindrical rather than Cartesian

coordinates. Since cylindrically symmetric problems do not depend on the azimuthal angle $\phi$ by definition, the Young–Laplace equation reduces to an ordinary differential equation. If we parameterize the surface by a function $r(z)$, the Young–Laplace equation becomes

$$\Delta P_L = 2\gamma \left( \frac{1}{rS} - \frac{\partial_{zz} r}{S^3} \right) \tag{1.9}$$

where $S = \sqrt{1 + (\partial_z r)^2}$.

### 1.2.2 Applications of the Young–Laplace Equation: The Rayleigh–Plateau Instability

The instability of a cylindrical liquid jet against breakup into a series of drops is one of the most common examples of a process that is entirely driven by surface tension. The physical principles encountered here are very generic and govern many drop formation processes in microfluidics, including, among others, EW-driven lab-on-a-chip systems. Figure 1.5a shows a series of snapshots of a free jet of one liquid in a second immiscible ambient liquid at different times ranging from zero to the final moment when the jet is broken up completely. As the images show, the decomposition starts with a small perturbation of a well-defined wavelength $\lambda$ of the initially perfectly cylindrical jet. This perturbation grows with time until the jet eventually breaks up into a combination of large drops located at the grown antinodes of the perturbation and – in this case – a number of smaller satellite drops located at the nodes of the original perturbation. Qualitatively, it is clear from the discussion above that the system reduces its interfacial energy by transforming the long and slender jet with a large surface-to-volume ratio into drops. In fact, one big drop would correspond to the absolute minimum of surface energy. But it is also intuitively plausible that forming one big drop is very unlikely because it would involve the transport of fluid over very long distances. Why is there a characteristic finite length wavelength of the perturbation? How

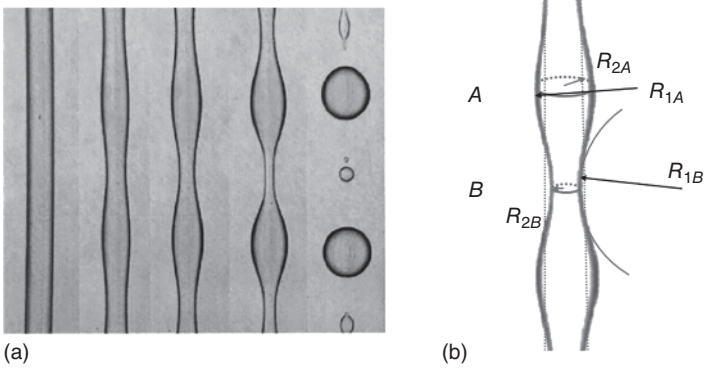


**Figure 1.5** (a) Snapshots of a cylindrical jet breaking up into drops with increasing time from left to right. Source: Reprinted with permission from [7]. (b) Illustration of the local curvature as a function of the perturbation.

does this length scale depend on the characteristic parameters of the problem? Why are there satellite droplets?

The answers to some of these problems require a detailed full analysis of the fluid dynamic problem. A first set of answers, however, can already be obtained by considering the variation of either the surface energy or the pressure distribution for small perturbations of the originally cylindrical jet. For the energy approach, all we need to do is calculate the surface area as a function of the amplitude and wavelength for one period of the perturbation. If it decreases with increasing amplitude, the perturbation will spontaneously grow. If it increases, capillary forces will restore the original unperturbed configuration. This very common mathematical approach is known as linear stability analysis. We start with small a periodic perturbation $\delta r(z) = \varepsilon \cos qz$, where $q = 2\pi/\lambda$ is the wavenumber of the perturbation and $\varepsilon \ll r_{cyl}$ is the initially small amplitude. The resulting surface profile of the jet is then given by $r(z) = r_{cyl}(\varepsilon) + \delta r(z)$. Here the average radius of the cylinder $r_{cyl}$ is a function of $\varepsilon$ because the total liquid volume must not depend on the amplitude of the perturbation. Imposing volume conservation leads to $r_{cyl}(\varepsilon) = (r_0^2 - \varepsilon^2/2)^{1/2} \approx r_0(1 - (\varepsilon/r_0)^2/4)$, where $r_0$ is the unperturbed initial radius. To calculate the surface area, we note that the area element on the surface is $dA = rd\phi(1 + (\partial_z r)^2)^{1/2}dz$. Integrating over one full period of the perturbation, we find to lowest order in $\varepsilon$

$$A(\varepsilon) = 2\pi r_0 \lambda \left(1 + \frac{\varepsilon^2}{4r_0^2}(q^2 r_0^2 - 1)\right) \tag{1.10}$$

Whether $A$ increases or decreases with increasing $\varepsilon$ thus depends exclusively on the term $(q^2 r_0^2 - 1)$. It is negative for small wavenumbers and positive for large ones. If $\lambda > 2\pi r_0$, i.e. if the wavelength of the perturbation is longer than the circumference of the original cylinder, the perturbation reduces the energy of the system. Vice versa, the energy increases for $\lambda < 2\pi r_0$. Qualitatively, this result should not surprise us. If the wavelength is very short, that is, $\lambda \ll r_0$, any perturbation can obviously only increase the surface area. In this case, the surface is effectively locally flat on the scale of the perturbation. Hence, introducing ripples can only increase the surface area and energy. Conversely we already argued that a sphere has the smallest surface-to-volume ratio. Hence, on large scales, it must be energetically favorable for the jet to decompose into drops. From the perspective of a linearized analysis of the energy balance, we can thus understand that perturbations above a certain wavelength are favorable. The characteristic wavelength separating the stable from the unstable regime is $2\pi r_0$. This is reasonably close to but at the same time clearly less than the length scale, as seen in Figure 1.5a.

Let us analyze the same problem from the perspective of the Young–Laplace equation, i.e. from the perspective of local force and pressure balances. As the radius of the cylinder becomes perturbed, the local radii of curvature $R_1$ and $R_2$ both vary along the jet. At point $A$, the antinode of the perturbation where $r(z)$ is maximum, $R_{1A}$ is positive, and at location $B$, the node, $R_{1B}$ is negative. $R_2$ is positive both at $A$ and at $B$. Yet, $R_{2A}$ increases with increasing amplitude of the perturbation, whereas $R_{2B}$ decreases. For small perturbations, it is easy to show that $1/R_{1A} = \partial_{zz} r(z)\,|_A = +\varepsilon q^2$. Similarly, $1/R_{1B} = -\varepsilon q^2$, i.e. the local radius

of curvature at $B$ in that plane is negative, as it should be (see Figure 1.5b). Since $R_2(z)$ is simply given by $r(z)$, we can write down after some algebra the local curvatures at $A$ and $B$ to lowest order in $\varepsilon$ as $\kappa_A = 1/r_0 \cdot (1 + \varepsilon/r_0 \cdot (r_0^2 q^2 - 1))$ and $\kappa_B = 1/r_0 \cdot (1 + \varepsilon/r_0 \cdot (1 - r_0^2 q^2))$. Hence, the pressure difference between $A$ and $B$ is

$$\Delta P = \Delta P_{L,A} - \Delta P_{L,B} = \frac{2\gamma\varepsilon}{r_0^2}(r_0^2 q^2 - 1) \tag{1.11}$$

In other words, the pressure in $A$ is larger than the pressure in B if $\lambda < 2\pi r_0$. In this case, the pressure gradient in the fluid will drive liquid back from the bulge of the perturbation to the neck, thus restoring the original shape. This is the stable configuration. Vice versa, for $\lambda > 2\pi\, r_0$ the pressure in $B$ is larger than in $A$, and therefore even more liquid will flow from the neck toward the bulge, thus allowing the perturbation to grow, in agreement with our conclusions above.

Both linearized energy analysis and linearized pressure balance thus yield the same information regarding the critical wavelength separating stable from unstable perturbation modes. To obtain fully quantitative predictions of the final breakup, we also need to consider dynamic aspects. To illustrate this, let us go back to Eq. (1.11). This equation tells us that the driving pressure difference will be larger and larger if we increase $\lambda$. One might therefore expect that the entire jet should transform into one big drop. This, however, would require transport of fluid over very large distances, which is dynamically very unfavorable. In fact, the quantity that drives the fluid flow is not the pressure difference between node and antinode but the pressure *gradient*. The pressure gradient, however, scales as $q \times \Delta P$ and therefore vanishes for $\lambda \to \infty$. The full hydrodynamic solution of the problem obtained independently by Rayleigh and Plateau in the nineteenth century shows that the fastest-growing perturbation has a wavelength $\lambda_{\max} = 9.02\, r_0$. This wavelength also sets the size of the drops in the final state. A detailed analysis of this problem can be found in standard textbooks of fluid dynamics [8].

## 1.3 Young–Dupré Equation: The Basic Law of Wetting

So far, we only considered interfaces between two fluid phases, liquid and vapor, or two immiscible liquids. Wetting is about contact between three different phases, in most cases a solid, a liquid, and a vapor phase. The latter can be replaced by a second immiscible liquid phase. Furthermore, we may also consider two immiscible liquids and vapor such as oil drops on a water surface, or even three immiscible liquids.

### 1.3.1 To Spread or Not to Spread: From Solid Surface Tension to Liquid Spreading

First of all, we note that the physical concept of a surface tension as we have introduced in Section 1.1 is not limited to liquids. Also for solids, molecules or atoms at the surface lack binding partners as compared with the bulk. Hence, solids equally

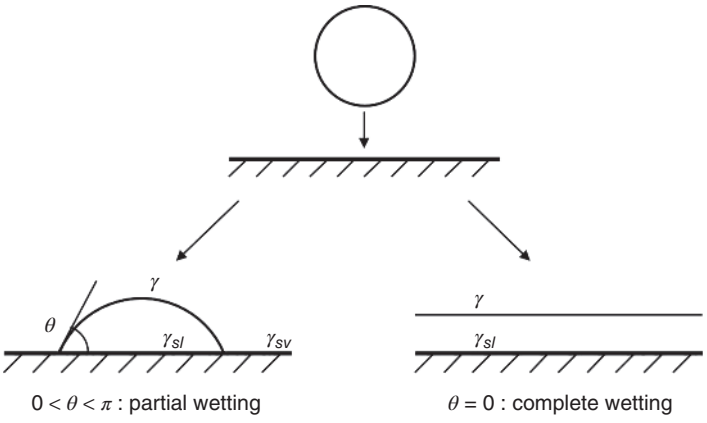


**Figure 1.6** Deposition of a liquid drop on a solid surface leads to either partial wetting (left) or complete wetting and spreading of the liquid into a thin film (right).

display surface and interfacial energies with adjacent phases. Since the origin of the surface energies is the same, it is also not a surprise that the order of magnitude of solid surface tensions is roughly the same as the one for liquids – higher cohesive energies for solids with covalent bonds pending. However, in contrast to liquids, solids also possess a finite elasticity that usually prevents noticeable deformations of solid surfaces due to surface tension forces. This circumstance makes the absolute measurement of the surface tension of solids rather difficult.

A basic wetting experiment starts with the deposition of a drop of liquid on a solid surface, as sketched in Figure 1.6. Following drop deposition, the liquid either spreads completely to form a liquid film that covers the entire solid surface, or it spreads only partially and forms a drop with a finite contact angle $\theta$. The former case is called complete wetting, and the latter partial wetting. If the surface is homogeneous, we can already anticipate from our considerations in the previous section that the drop will assume a spherical cap shape to guarantee a constant pressure everywhere inside the liquid.

At first glance, complete wetting may seem physically less interesting and practically less relevant. Yet, this is not the case. In fact, complete wetting is very desirable in many situations including in particular coating technology and lubrication. Complete wetting with zero contact angle is a prerequisite to achieve a thermodynamically stable films on top of a solid surface. In systems involving two immiscible fluid phases such as water and oil in many EW experiments, complete wetting of the continuous phase allows for keeping the dispersed drop phase separated from the solid surfaces by a thin oil film that can lubricate the motion of the drop and reduce the fouling of solutes onto a solid substrate. Partial wetting with a finite contact angle, on the other hand, is *the* generic situation scenario in standard EW experiments.

To understand the difference between complete and partial wetting, we consider the macroscopic energy of the system before and after the deposition of the drop. As previously, the equilibrium is determined by the minimum of the free energy of the system. If the substrate surface is very large and the drop volume is

rather small, the energy in the initial state is essentially the solid–vapor interfacial energy, i.e. $G_i \approx A_{sv}\,\gamma_{sv}$. Here, the solid–vapor interfacial area $A_{sv}$ is identical with total the surface area $A$ of the solid. For partial wetting, total surface energy of the system is basically not affected by the deposition of the drop because the drop–substrate and the drop–vapor interfacial area are negligibly small compared with $A_{sv}$. In contrast, for complete wetting, the solid–vapor interface is replaced by two macroscopic interfaces, namely, the solid–liquid interface and the liquid–vapor interface. Hence, the surface energy in the final state is $G_f = \gamma\, A_{lv} + \gamma_{sl} A_{sl} = A(\gamma + \gamma_{sl})$. The difference between the two normalized by the surface area is known as the spreading parameter:

$$S = \frac{G_i - G_\mathrm{f}}{A} = \gamma_{sv} - (\gamma_{sl} + \gamma) \tag{1.12}$$

If $S > 0$, the solid–vapor interface is energetically unfavorable compared with the sum of solid–liquid and liquid–vapor interface. Hence, the liquid spreads to a thin film covering the entire surface, i.e. the system displays complete wetting. Vice versa, for $S < 0$, localizing the liquid in a partially wetting drop with a finite contact angle is energetically more favorable.

A simple gedankenexperiment allows us to relate the occurrence of complete and partial wetting to the relative strength of the various molecular interaction forces. Let us consider a block of some material $\alpha$, as sketched in Figure 1.7. We cleave the block into two halves. From a macroscopic perspective, the difference between the initial state and the final state is simply the existence of two additional surfaces of area $A$ of material $I$, with a corresponding surface energy $\gamma_I$. Assuming that we can cleave the block without any energy losses due to dissipation, the work we performed in the process is $\delta W_{I-I} = 2\gamma_I A$. From a microscopic perspective, we broke the bonds between adjacent molecules everywhere along the cleavage plane. This means that we effectively transferred molecules from the minimum $U_{I-I}(a)$ of their molecular interaction potential in the bonded state to infinity, where the molecular interaction potential vanishes, $U_{I-I}(\infty) = 0$. Hence, we have $2\gamma_I = U_{I-I}$. If we repeat the same experiment with the same kind of experiment for a block of two different materials $I$ and $II$ that are initially in contact, cleavage eliminates an $I$–$II$ interface in the initial state and creates instead an $I$-surface and a $II$-surface. Hence, we have macroscopically $\delta W_{I-II} = \gamma_I + \gamma_{II} - \gamma_{I-II}$. Microscopically, we separated the $\alpha$- and $\beta$-molecules at the interface from their original minimum interaction energy $U_{I-II}$ to infinity, i.e. $\delta W_{I-II} = U_{I-II}$.

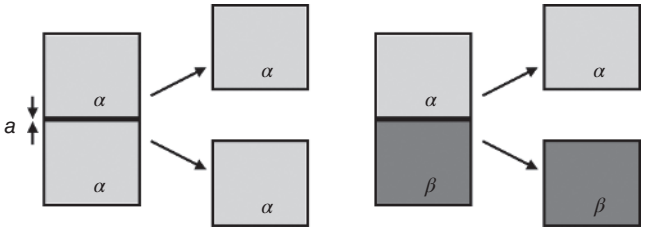


**Figure 1.7** Gedankenexperiment of cleaving a homogeneous block of material $\alpha$ (left) and a heterogeneous block $\alpha/\beta$ (right) into two separate blocks.

If we now identify $\alpha$ with the solid $s$ and $\beta$ with the liquid $l$ in a wetting experiment, we can express the spreading parameter in terms of the molecular interaction energies as

$$S = \gamma_{sv} - (\gamma + \gamma_{sl}) = U_{sl}(a) - U_{ll}(a) \tag{1.13}$$

We find thus a very natural result: Complete wetting, $S > 0$, occurs whenever the molecular interaction of the molecules of the solid with the molecules of the liquid is stronger than the interaction among the molecules of the liquid. In the opposite case, $S < 0$, partial wetting occurs. For the ubiquitous van der Waals forces, we can go even one step further: van der Waals interaction between two molecules is caused by the coupling of spontaneous fluctuations of the electron cloud of one molecule to the induced dipole moment of the other. Hence, van der Waals interaction is proportional to the polarizabilities $\alpha$ of both molecules: $U_{I-II\,vdW} \propto \alpha_I\ \alpha_{II}$. Inserting this into our expression Eq. (1.13), we find $S \propto \alpha_l\ (\alpha_s - \alpha_l)$. Hence, in the case of pure van der Waals interaction, liquids completely wet any solid with a higher polarizability. This result leads to the conclusion that liquid helium, the chemically most inert material that interacts only via van der Waals interaction and displays the lowest polarizability of all materials, should wet any solid. This was found to be generally true. (Interestingly, the alkali metals Cs and Rb provide an exception to this rule because the specific electronic structure of these materials leads to an initially unexpected quantum mechanical contribution to the interaction forces that dominates over van der Waals interaction.)

### 1.3.2 Partial Wetting: The Young Equation

Complete wetting systems involve three different phases. Yet, one of the phases separates the two others completely such that there are only two types of interfaces. In partial wetting all three combinations of interfaces exist. Moreover, there is a one-dimensional region, the edge of the drop, where all three phases involved meet. For obvious reasons, this region is called the three-phase contact line, or shorter, the contact line. Since the three interfaces meet, we can define – within each phase – the angle between the two adjacent phases. For the generic case of a flat surface, the angle between the *sv* interface and the *sl* interface is 180° by definition. For a liquid drop in ambient vapor, the angle between the *sl* and the *lv* interface is known as the contact angle of the liquid. It is typically denoted as Young's angle $\theta_Y$, honoring the English physicist Thomas Young (1773–1829). The complementary angle between the *sv* and the *lv* interface is obviously $\pi - \theta_Y$. Like in the case of the sign convention of the radius of curvature, we should note that the definition is not necessarily unique. In particular for liquid–liquid systems, it is important to define properly through which phase *the* contact angle is measured. For now, we will think of a liquid drop in ambient vapor and speak about the angle measured in the liquid phase. Our primary concern is to understand how the contact angle $\theta_Y$ is related to the three interfacial tensions in the system. Since $\theta_Y$ is an equilibrium property, it is clear that it must be determined by the minimum of the total (surface) energy for any given fixed drop volume.

The total surface energy of a sessile drop is given by the sum of all the interfacial energies:

$$E_{surf}[\mathrm{A}] = \sum_i A_i \gamma_i \tag{1.14}$$

Here the sum $i$ runs over all three types of interfaces, namely, solid–liquid ($sl$), solid–vapor ($sv$), and liquid–vapor ($lv$) – the index that we usually suppress. The area of the solid–vapor interface is given by $A_{sv} = A_{tot} - A_{sl}$, the total surface area of the substrate minus the solid–liquid interfacial area. The former can be neglected because it provides only a constant offset that does not depend on the drop shape. Neglecting this irrelevant contribution, we can rewrite Eq. (1.14) as

$$E_{surf}[A] = A_{lv}\gamma + A_{sl}(\gamma_{sl} - \gamma_{sv}) \tag{1.15}$$

$E_{surf}$ is a functional of the shape $A$ of the drop, which is determined by $A_{lv}$ and $A_{sl}$. $A$ is thus the unknown function that minimizes the functional $E_{surf}$. Finding functions that minimize functionals is the general subject of variational calculus. We will describe this somewhat elaborate formalism in detail in Section 1.5.

Here, we focus on the vicinity of the contact line. On this local scale, the curvature of the liquid–vapor interface is negligible, and hence drop surface can be considered as flat, as shown in Figure 1.8. As we already did before, we consider the problem first from the perspective of energy minimization and subsequently from the perspective of local force balance. If the drop is in an equilibrium configuration that minimizes the surface energy, the variation of the surface energy $\delta E_{surf}$ upon displacing the contact line by a small amount must vanish. If we displace the contact line by $dx$, say, to the left, as sketched in Figure 1.8a, we convert $sv$ interface into $sl$ interface along $dx$. Moreover, we generate a little extra piece of liquid–vapor interface with the length $dx\cos\theta$. The resulting variation of the interfacial energy is given by

$$\delta E_{surf} = dx\,(\gamma_{sl} - \gamma_{sv} + \gamma\cos\theta) \tag{1.16}$$

**Table 1.2** Geometric functions characterizing spherical caps and circles.

| | | |
|---|---|---|
| 3D | $V(R,\theta) = \frac{\pi}{3}R^3(1-\cos\theta)^2(2+\cos\theta)$ | 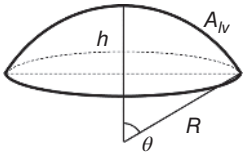 |
| | $r_{sl}(R,\,\theta) = R\sin\theta$ | |
| | $A_{sl}(R,\,\theta) = \pi R^2\sin^2\theta$ | |
| | $A_{lv}(R,\,\theta) = 2\pi R^2(1-\cos\theta)$ | |
| | $h(R,\,\theta) = R\,(1-\cos\theta)$ | |
| 2D | $A = \frac{R^2}{2}(2\theta - \sin 2\theta)$ | 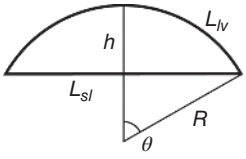 |
| | $L_{sl} = 2R\sin\theta$ | |
| | $L_{lv} = 2R\,\theta$ | |
| | $h = R(1-\cos\theta)$ | |

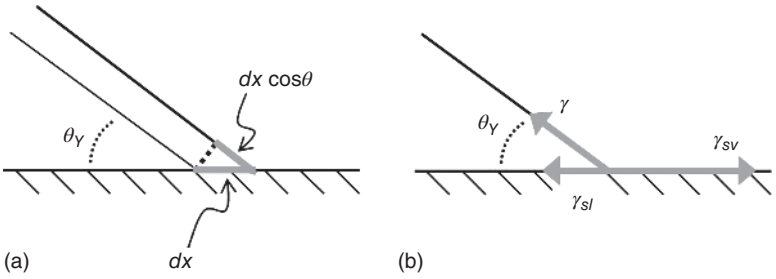


**Figure 1.8** (a) Illustration of the variation in interfacial areas upon displacing the contact line by *dx*. (b) Force balance at the contact line.

Equating $\delta E_{surf}$ to zero we find the desired relation between the equilibrium contact angle $\theta_Y$ and the three interfacial tensions in the system, the Young–Dupré equation:

$$\cos\theta_Y = \frac{\gamma_{sv} - \gamma_{sl}}{\gamma} \tag{1.17}$$

Upon inspecting the Young–Dupré equation, or simply *Young's* equation, we can immediately make a couple of simple observations: First of all, for $\gamma_{sl} = \gamma_{sv}$, we find $\theta_Y = 90^{\circ}$. This is natural because the creation of solid–liquid and solid–vapor interfacial area is equally costly under these conditions. That is, the solid has no preference for either of the two phases. If solid–vapor interface is more costly than solid–liquid interface, $\theta_Y$ is smaller than 90° and vice versa. Note also that the value of $\cos\theta_Y$ is bounded between −1 and +1, whereas the value of the RHS of Eq. (1.17) is not. This is not a problem. We derived Eq. (1.17) under the explicit assumption that the system *is* in the partial wetting regime. If $\theta_Y$ reaches a value of either 0° or 180°, the basic assumption underlying the derivation no longer holds. This simply means that the system undergoes a transition from partial wetting to complete wetting of one of the two phases.

As we discussed in the preceding sections, we can equivalently interpret interfacial tensions as tensile forces per unit length within the interface. When we discussed the force-based macroscopic definition of the interfacial tensions in the context of Figure 1.2, we already noticed what happens when a liquid surface with a surface tension ends on a solid surface: The tension is transmitted as a force per unit length of the contact line. Likewise, the liquid–vapor interface along the edge of our drop pulls on the three-phase contact line with its tension tangential to the liquid–vapor interface, as sketched in Figure 1.8b. In the same fashion, the solid–liquid and the solid–vapor interfacial tension pull on the contact line along their respective directions. In mechanical equilibrium, all forces must balance. Otherwise the contact line would start to move along the surface. Projecting $\gamma$ onto the horizontal direction and adding the two other interfacial tensions, we recover Young's equation, Eq. (1.17), from the balance of the horizontal components of the interfacial tensions at the contact line.

In the force balance picture, we can easily understand the transition from partial wetting to complete wetting. Suppose we gradually increase $\gamma_{sv}$ by some process or $\gamma_{sl}$ decreases as it effectively does in EW upon applying a voltage. In this case the contact angle has to decrease to align the direction of $\gamma$ better with

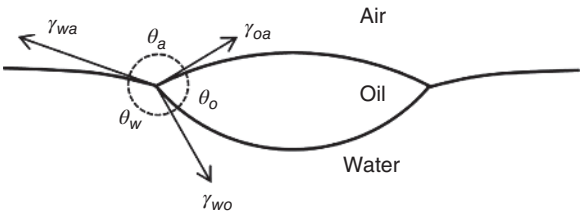


**Figure 1.9** Schematic illustration of the force balance at contact line of an oil drop floating on water.

solid–liquid interface in order to preserve force balance. Eventually, $\theta_Y$ will have decreased to zero and even the fully aligned $\gamma_{sl}$ and $\gamma$ together are no longer able to balance the tension of the solid–vapor interface. This is the critical condition when the spreading parameter $S$ (see Eq. (1.12)) vanishes and the liquid undergoes the transition from partial to complete wetting. Such a transition is known as wetting transition. Wetting transitions are thermodynamic phase transitions. They are typically driven by gradual variations of interfacial tensions with an external control parameter such as temperature of the chemical composition of one of the phases.

The reader may also wonder about the force balance in the direction normal to the solid surface. Obviously, the surface tension of the liquid also pulls in that direction with a force per unit length of $f_\perp = \gamma \sin\theta$. This component is balanced by elastic restoring forces of the solid substrate. Under normal circumstances, i.e. with typical *hard* substrate materials such as glass, this deformation is extremely small and for all practical purposes negligible. The characteristic length scale of these deformations is given the ratio of the surface tension divided by the elastic modulus $G$ of the solid. For typical hard solids $G$ is of the order of several gigapascal. Dividing a typical surface tension of $0.1\,\mathrm{J\,m^{-2}}$ by, say, 10 GPa, we obtain a characteristic length of $10^{-11}$ m. For softer substrates, such as weakly cross-linked polymers (e.g. polydimethylsiloxane (PDMS)) with $G \approx 10^5$ Pa, recent experiments showed that the surface tension-induced deformation of the substrate can indeed be finite [9]. The most extreme example of a *soft* substrate is another liquid. Indeed, everyday kitchen experience tells us that small oil drops floating on water pull the water surface upward around the contact line. In this case, the oil–water (ow) interface, the water–air (wa) interface, and the oil–air (oa) interface are all deformable. Balancing all three surface tension forces at the contact line leads to the so-called Neumann triangle relating the three characteristic angles to the three interfacial tensions involved:

$$\frac{\gamma_{oa}}{\sin\theta_w} = \frac{\gamma_{wa}}{\sin\theta_o} = \frac{\gamma_{ow}}{\sin\theta_a} \tag{1.18}$$

Here, the subscripts of the angles indicate the phase in which the angle is measured. See Figure 1.9 for an illustration of the definitions. Useful geometric relations of spherical caps are given in Table 1.2.

## 1.4 Wetting in the Presence of Gravity

So far, we discussed wetting systems in the presence of surface tension forces only. In practice, other forces such as gravity and in EW electrostatic forces are

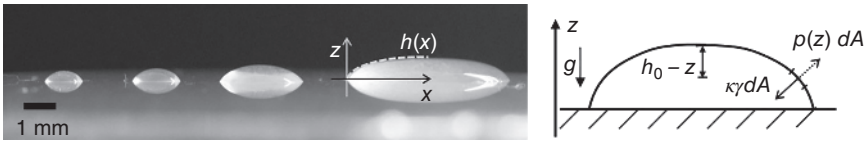


**Figure 1.10** (a) Sessile water drops of variable size on a polymer substrate. (b) Schematic of sessile drop illustrating inward- and outward-oriented forces on a surface element *dA*.

omnipresent. From daily experience, we are familiar with the effect of gravity. While small sessile drops assume spherical cap shapes on homogeneous surfaces as discussed above, larger drops assume the shape of puddles that are flat on the top; see Figure 1.10. Daily experience tells us that the transition from the capillarity-dominated regime of spherical caps to the gravity-dominated regime of flattened puddles takes place on a characteristic length scale of a few millimeters, which is known as capillary length $\lambda_c$. The exact value of $\lambda_c$ depends on the properties of the liquid. Yet, it turns out that the order of magnitude of a few millimeters actually holds for the majority of common liquids. In this section we demonstrate how external forces can be incorporated into the laws of wetting and capillarity as we have discussed them so far. Specifically, we want to understand the origin of the capillary length, and we want to derive a quantitative formalism that allows us to calculate equilibrium drop surface profiles $h(x)$ in the presence of gravity, as shown in Figure 1.10a.

To understand heuristically the effect of gravity on the equilibrium shape of drops, we return to our discussion of the derivation of the Young–Laplace equation based on force balance. A key element in our derivation was the point that the pressure $p$ within the drop is constant and equal to the pressure drop $\Delta P_L = \gamma\kappa$ across the surface. In the presence of gravity, however, the pressure within the liquid is no longer constant but increases with increasing depth below the surface due to the hydrostatic pressure. Every volume element $dV$ of liquid experiences a gravitational body force $d\vec{f}_g = -\rho g dV \vec{e}_z$. At a depth $\Delta h = h_0 - z$ below surface, this *directional* gravitational force gives rise to an *isotropic* hydrostatic pressure $p(z) = p_0 - \rho g z$. ($h_0$ and $p_0$ denote the highest position of the liquid surface and the reference pressure at that height.) (In Appendix 1.A to this chapter, we provide a somewhat more formal discussion of these considerations introducing a description in terms of the stress tensor that is also relevant for electric fields in EW.) Qualitatively, any surface element $dA$ experiences an outward-oriented force $p(z)dA$ that is balanced by the inward-oriented surface tension force $\kappa\gamma\, dA$, as illustrated in Figure 1.10b. In the presence of gravity, the original Young–Laplace equation in three-dimensional space is thus replaced by

$$2\gamma\kappa = p_0 - \rho g z \tag{1.19}$$

(The factor 2 applies for three-dimensional systems.) If we write the equation in this manner, we assume that the density in the ambient phase is negligible. If this is not the case, the hydrostatic pressure in the ambient phase also varies with $z$ according to the density $\rho_a$ of the ambient fluid. In this case, $\rho$ in Eq. (1.19) has

to be replaced by $\Delta\rho = \rho - \rho_a$. Note that $\Delta\rho$ can be either positive or negative, depending on the relative densities of the drop phase and the ambient liquid.

The gravitational body force thus appears as an additional term in the Young–Laplace equation. As we will demonstrate explicitly in a more formal derivation in Section 1.5, gravity does not appear in the balance of forces at the contact line. Gravity thus distorts the surface of the drop but does not affect the contact angle. In Chapter 5, we will see that the same applies for electric fields in the context of EW if we look sufficiently closely in the vicinity of the contact line.

### 1.4.1 Bond Number and Capillary Length

Before analyzing the specific problem of the shape of the puddle in some detail, we estimate the relative importance of the three terms in Eq. (1.19). To do so, we need to identify the characteristic parameters of the problem and rewrite the equation in nondimensional units. The radius $R$ of the drop is obviously a characteristic length scale. If necessary, we can define $R$ based on the cube root of the liquid volume. Hence, we can use $R$ to define a nondimensional height $\tilde{z} = z/R$. Since the curvature has the dimension of an inverse length, we have $\tilde{\kappa} = R\kappa$. The characteristic value of the capillary pressure is $\gamma/R$. This leads to a nondimensional pressure $\tilde{p} = p\,R/\gamma$. With these definitions and after rearrangement of the terms, the nondimensional version of Eq. (1.19) becomes

$$\tilde{p} = 2\tilde{\kappa} + \frac{\rho g R^2}{\gamma}\tilde{z} = 2\tilde{\kappa} + Bo\,\tilde{z} \tag{1.20}$$

Since $\tilde{z}$ and $\tilde{\kappa}$ have numerical values of order unity, we see immediately that the gravity term dominates if $Bo = \rho g R^2/\gamma$, the *Bond number*, is large compared with unity and vice versa capillary forces dominate for $Bo \ll 1$. For $Bo = 1$, gravity and capillarity are equally important. Since $Bo$ scales as $R^2$, we find what we expected: Gravity is negligible on small scales and dominates on large scales. Using the definition of $Bo$, we can identify a characteristic length scale, the capillary length

$$\lambda_c = \sqrt{\frac{\gamma}{\rho\, g}} \tag{1.21}$$

$\lambda_c$ is *the* characteristic length in any problem involving capillary forces and gravity. It defines the transition from the capillarity-dominated small scales to the gravity-dominated large scales. Inserting numbers for water, we find $\lambda_c = 2.3$ mm. Since $\lambda_c$ depends only on the square root of the ratio of surface tension and density, it turns out that $\lambda_c$ almost universally adopts a value of order 1 mm for all common liquids, as can be verified by inserting the surface tensions and densities tabulated in Table 1.1. Much larger values are realized in space. For this reason many fundamental experiments to test the laws of capillary have actually been carried out in space. On Earth, the easiest manner to achieve large values of the capillary length is to use liquid–liquid systems with matched densities of the two phases. (In this case, the density $\rho$ in the expression for $\lambda_c$ is again replaced by $\Delta\rho$, as noted above.) Taking specific care, e.g. by tuning using mixtures of solvent or by adding solutes densities of oil and water, can be matched up to a precision of $\Delta\rho \approx 10^{-3}\rho$. This leads to values of $\lambda_c$ of several centimeters. This is, for instance,

crucial for optimizing the design of (e.g. EW-driven) optofluidic devices such as tunable lenses and beam deflectors that we will discuss in Chapter 8. Note that matching the densities of liquids not only reduces the effect of gravity, but it also reduces the effect of inertial forces. As a consequence density-matched optofluidic devices are particularly insensitive to mechanical shocks and vibrations.

### 1.4.2 Case Studies

#### 1.4.2.1 The Shape of a Liquid Puddle

What is the equilibrium shape of the liquid puddles shown in Figure 1.10, and what is their height $h_\infty$ far away from the contact line? Let us assume that the puddle is very large (i.e. $R \gg \lambda_c$) such that it becomes completely flat far away from the contact line. In this limit it is reasonable to consider the one-dimensional version of Eq. (1.19), i.e.

$$-\gamma \frac{h''}{(1+h'^2)^{\frac{3}{2}}} = p_0 - \rho g\, h \tag{1.22}$$

where the prime indicates a derivative with respect to $x$ (cf. Eq. (1.7)). Note the minus sign on the left-hand side (LHS) that ensures a positive pressure inside the drop. Since we assume the puddle to become flat far away from the contact line, we know that $h''(x), h'(x) \to 0$ for $x \to \infty$, while $h(x) \to h_\infty$. From this boundary condition, we can infer immediately that $p_0 = \rho g h_\infty$. Furthermore, we know that the slope of the surface at the contact line must correspond to Young's angle, i.e. $h'(0) = \tan\theta_Y$. Equation (1.22) is an ordinary nonlinear second-order differential equation for the surface profile $h(x)$. Noting that $h''/(1+h'^2)^{3/2} = d/dx(h'/(1+h'^2)^{1/2})$, we can integrate Eq. (1.22) once to obtain

$$(\cos\phi(x) - \cos\theta_Y) = \frac{h(x)\left(h_\infty - \frac{h(x)}{2}\right)}{\lambda_c^2} \tag{1.23}$$

Here, $\phi(x)$ with $\cos\phi = 1/\sqrt{1+h'^2}$ is the local slope angle of $h(x)$, as indicated in Figure 1.11. Equation (1.23) is now a first-order differential equation for $h(x)$. It can be integrated numerically to obtain the full profile.

While there is no analytical solution for $h(x)$, we can nevertheless deduce some useful information from Eq. (1.23). In particular, we can calculate the height $h_\infty$ of a puddle without calculating the full profile by considering the limit $x \to \infty$. In this limit $\phi \to 0$ and $h \to h_\infty$. Inserting these boundary conditions in Eq. (1.23), we obtain after a little algebra

$$h_\infty = 2\lambda_c \sin\frac{\theta_Y}{2} \tag{1.24}$$

The thickness of a liquid puddle is thus independent of its size, in agreement with daily experience. Moreover, we find that $h_\infty$ is given by a combination of the wettability of the surface and $\lambda_c$. Thus, $\lambda_c$ appears prominently in this capillarity-/gravity-dominated problem, as anticipated above.

Next to the formal manner of solving the Young–Laplace equation discussed above, we can also arrive at Eq. (1.23) directly by balancing the horizontal component of all external forces acting on the various control volumes shaded in gray

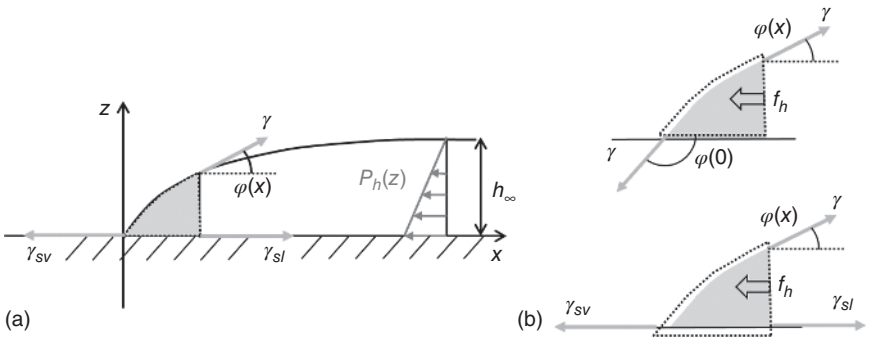


**Figure 1.11** Surface profile of a puddle of liquid. (a) Global view indicating the height-dependent pressure. (b) Two alternative selections of the control volume with the bottom just above (top) and just below (bottom) the solid–liquid interface.

in Figure 1.11. In mechanical equilibrium, the sum of all forces acting on a control volume must obviously add up to zero. The details of the calculation depend on our specific choice of the control volume. Let us first consider the gray-shaded control volume in the bottom of Figure 1.11b, which is a zoomed view of the one shown in Figure 1.11a. The lower boundary is chosen inside the solid substrate just below the solid–liquid interface, and the curved boundary follows the surface profile just outside the liquid. The right vertical boundary connects the ends of the two other sections. With this choice, the boundary of the control volume crosses the solid–liquid, the liquid–vapor, and the solid–vapor interface. At every intersection with an interface, the corresponding interfacial tension pulls tangentially along the direction of the interface, as indicated in the figure. In addition to the surface tension forces, the liquid experiences the hydrostatic pressure force from the liquid column along the right boundary of the control volume. This force is given by

$$f_h = \int_0^{h(x)} (\Delta p - \rho g\, z)\, dz = \rho g\, h(x)\, (h_\infty - h(x)/2)$$

Balancing horizontal components of all forces, we arrive at the equation

$$\gamma_{sl} + \gamma \cos \phi(x) = \gamma_{sv} + \rho g h(x)(h_\infty - h/2) \tag{1.25}$$

Using Young's equation to eliminate $\gamma_{sl}$ and $\gamma_{sv}$, we recover Eq. (1.23). Alternatively, we could have chosen the bottom edge of the control volume in the liquid phase, just above the solid–liquid interface, as shown in the top of Figure 1.11b. In this case, the surface of the control volume intersects neither with the solid–liquid nor with the solid–vapor interface. Instead, there is a second intersection with the liquid–vapor interface close to the contact line, where the slope of the surface profile corresponds to Young's angle. Inserting this boundary condition, we find that the net surface tension force acting on the control volume is $f_\gamma(x) = \gamma(\cos\phi(h(x)) - \cos\theta_Y)$. Balancing this expression with the pressure force $f_h$, we recover again Eq. (1.23).

#### 1.4.2.2 The Pendant Drop Method: Measuring Surface Tension by Balancing Capillary and Gravity Forces

The competition between gravity and capillary forces provides us with a very convenient and accurate method to measure the surface tension of a liquid or the interfacial tensions between two liquids. In principle, $\gamma$ can be obtained by fitting the numerical solution of Eq. (1.23) to the shape of a puddle. If the density of the liquid is known, $\gamma$ and $\theta_Y$ are the only free parameters. In practice, this approach is not very convenient because puddles need to be rather large in diameter, and they tend to display rather small curvatures, in particular if the contact angle is small. Additional uncertainties arise if the solid surface is not perfectly homogeneous. These problems can be avoided if we simply hang a drop of liquid from the needle of a syringe, as shown in Figure 1.12. If the drop radius $R$ is small compared with $\lambda_c$, the drop is perfectly spherical. Upon gradually increasing the volume, the drop gets more and more deformed under the influence of gravity as $R$ becomes comparable to $\lambda_c$. At some point, the drop becomes too heavy and falls off the needle. This simple experiment offers two possibilities to measure surface tension. First of all, the falling drop has a well-defined volume that is determined by the maximum capillary force at the interface between the needle and the drop. The capillary force holding the drop on the needle is given by $f_\gamma = 2\pi r\gamma \cos\phi$, as illustrated in Figure 1.12. Obviously, this force has a maximum value of $f_\gamma = 2\pi r\gamma$ for $\phi = 0$. Since the weight of the drop is $f_\gamma = 4/3\pi R^3 \rho g$, balancing the two forces yields a drop radius of $R^* = \lambda_c(3r/2\lambda_c)^{1/3}$, where $r$ is the radius of the needle. By measuring the weight of the falling drops, we can thus determine the surface tension. In principle, this sounds very easy. Yet, the problem is that only a part of the originally unstable drop ends up falling. A finite fraction – up to 40% – remains stuck on the needle. The exact value depends on the details of the detachment dynamics and on the viscous properties of the liquid. This limits the accuracy of the measurements.

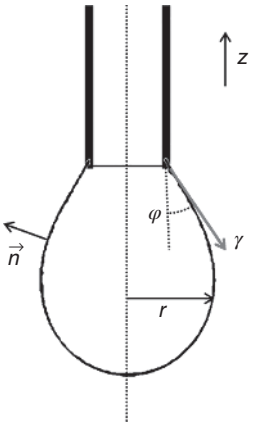


**Figure 1.12** Pendant drop hanging from a needle deformed under the influence of gravity. $\vec{n}$ is the surface normal unit vector.

The second much more reliable method is to determine the equilibrium shape of the drop under static conditions before it falls off the needle. In this case, we can fit the numerical solution of the capillary equation in cylindrical coordinates (Eq. (1.19)) to the measured shape of the drop. Knowing the needle radius $r$ and the liquid density, $\gamma$ is the only fit parameter in this procedure. Since both the acquisition of digital images and numerical fitting are nowadays performed on computers very easily and accurately, this so-called pendant drop method is one of the most popular methods for interfacial tension measurements. A practical added value is that the measurement can be done conveniently in the same instrument as a contact angle measurement.

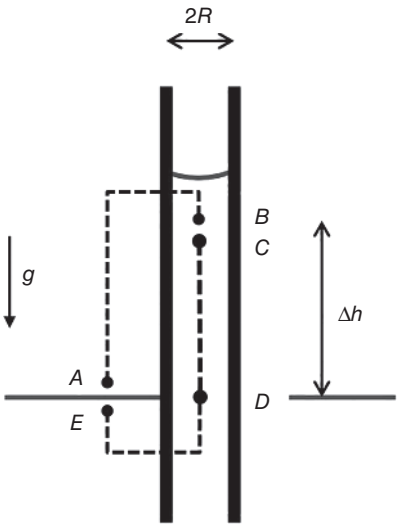


**Figure 1.13** Capillary rise in thin tube.

#### 1.4.2.3 Capillary Rise

The final example to be discussed is capillary rise. Capillary rise describes the phenomenon of liquid that is pulled upward into a thin capillary against the direction of gravity as sketched in Figure 1.13. The thinner the capillary, the higher the liquid rises. This is only true if the contact angle of the liquid on the surface is less than 90°. For $\theta_Y > 90^{\circ}$, the opposite phenomenon, capillary depression, is observed. A substantial height of rise (or depression) is only important for capillary diameters $2R \ll \lambda_c$. The problem of calculating the equilibrium height can be analyzed in many ways.

First, we analyze the variation of the pressure along the path indicated by the dashed lines and the points $A$–$E$ in Figure 1.13. The pressure in the ambient air at point $A$ is $p(A) = p_0$. If we neglect the density of the air, the pressure at point $B$ is the same, i.e. $p(B) = p(A)$. As we cross the air–water interface between $B$ and $C$, the pressure jumps due to the curvature of the interface. For a circular tube of radius $R$ and contact angle $\theta_Y < 90°$, we have $p(C) = p(B) - 2\gamma \cos\theta / R$. Here, we implicitly assumed that the liquid meniscus is spherical. This is justified as long as $2R \ll \lambda_c$. Moving from point $C$ to $D$, the pressure increases due to the hydrostatic pressure: $p(D) = p(C) + \rho g h$. $D$ and $E$ are at the same level. Hence, $p(D) = p(E)$. Since the surface of the liquid bath is flat, there is no pressure jump at that interface: i.e. $p(E) = p(A)$. Combining all these expressions, we find the height of capillary rise

$$h = \frac{2\gamma \cos\theta_Y}{\rho g R} \tag{1.26}$$

This equation is known as Jurin's law.

This derivation is very easy. Yet, it tends to hide the true physical driving forces of the process. The pressure jump across the meniscus is merely a consequence of the boundary condition $\theta_Y$ that we imposed on the liquid along the edge of the meniscus. The actual microscopic force driving the process is the difference

between $\gamma_{sv}$ and $\gamma_{sl}$. Since $\theta_Y < 90^\circ$, the capillary prefers to be wetted by water rather than by the ambient air. The role of this actual driving force appears more explicitly if we derive Jurin's law by considering the sum of all the forces acting on the liquid column inside the capillary from the level of the bath up to the meniscus. Along the three-phase contact line at the meniscus, the solid–vapor interfacial tension pulls upward with a total force $f_{sv} = 2\pi R\gamma_{sv}$. Along the edge of the lower end of the control volume at the level of the bath, the solid–liquid interfacial tension pulls downward with a force $f_{sl} = -2\pi R\gamma_{sl}$. Finally, there is the body force $-\rho g dV$ that pulls on each volume element of liquid. Integrating over the entire column, this leads to $f_g = -\pi R^2 h\rho g$. Adding up all the terms yields

$$2\pi R\gamma_{sv} = 2\pi R\gamma_{sl} + \pi R^2 h\rho g \tag{1.27}$$

Using Young's equation to replace $\gamma_{sv} - \gamma_{sl}$ by $\gamma\cos\theta_Y$, we recover Jurin's law. From this derivation it is very clear that the actual driving force is the difference of the interfacial tensions $\gamma_{sv}$ and $\gamma_{sl}$. This observation has an important consequence. It implies that the actual force pulling in the liquid does not depend on the curvature of the meniscus. Even if the liquid were frozen such that the meniscus would remain flat, it would still be pulled upward by the same force. If there were no friction, we would expect the same height of rise. In this sense, the fact that the liquid meniscus becomes curved is *merely* a consequence of the characteristic response of liquids to interfacial tension forces and to the specific geometry. The same argument has played an important role in early discussions of the origin of the ponderomotive forces responsible for the actuation of drops in EW and its relation to the variations of the contact angle. We will come back to this discussion in Chapter 5.

It is worth noting that wetting as a driving force for the penetration of confined spaces is important in a much broader context than capillary rise. Capillary forces also suck liquids into porous media, such as rock, paper, and textiles if the liquid wets the walls. The narrower the pores, the stronger the suction pressures. This phenomenon is known as *wicking*. The same process also gives rise to liquid fingers spreading in the corners of rectangular microfluidic channels. Conversely, very large pressures are needed to force liquid into narrow pores with contact angles on the walls exceeding 90°.

## 1.5 Variational Derivation of the Young–Laplace and the Young–Dupré Equation

As mentioned above, the two basic laws of wetting, Laplace's law and Youngs law, can both be derived in a consistent manner from the principle of energy minimization. The conceptual approach is similar to the minimization of some ordinary function of a set of variables, say, $f(x, y, z)$. A necessary condition to have a minimum (or maximum) some point $(x_0, y_0, z_0)$ is the requirement that the gradient of $f$ vanishes, i.e. $\nabla f(x_0, y_0, z_0) = 0$. To find extrema of functions, we therefore generally solve this condition for $(x_0, y_0, z_0)$. The minimization problem of the surface energy is similar, except that $E_{surf}$ is not simply a function

of a set of variables, but it depends on the shape $A$ of the liquid surface. For instance, we can parameterize $A$ by a function $h(x, y)$. $E_{surf}$ a function of the function $h(x, y)$, is called a functional. The analogue of our criterion $\nabla f(x_0, y_0, z_0) = 0$ is a differential equation that the equilibrium shape, the function $h_0(x, y)$, has to fulfill for $E_{surf}[h_0(x, y)]$ to be minimum. This equation is given by equating the first *functional* or *variational* derivative to zero, i.e. $\delta E_{surf} = 0$. As we will see in the end, there are in fact two equations that $h(x, y)$ has to fulfill, namely, the Young–Laplace and the Young–Dupré equations, Eqs. (1.6) and (1.17). Both basic equations thus arise directly from the same energy minimization procedure. Like in the case of an ordinary function, solving a specific problem then implies solving Laplace's equation and Young's equation for the equilibrium function $h_0(x, y)$ subject to specific boundary conditions. This is the general concept. The remainder of this section is somewhat technical and may be skipped by readers who are satisfied with understanding the general background.

In Eq. (1.15) we already noted that the surface energy of a sessile drop with a finite contact angle can be written as $E_{surf}[A] = A_{lv}\gamma + A_{sl}(\gamma_{sl} - \gamma_{sv})$. We can rewrite this expression in an integral form as

$$E_{surf}[A] = \int \gamma \, dA_{lv} + \int (\gamma_{sl} - \gamma_{sv}) dA_{sl} \tag{1.28}$$

We seek the minimum of this functional for a fixed volume $V$ of the drop. This constraint is included by minimizing the functional

$$G[A] = E_{surf}[A] - \lambda V \tag{1.29}$$

Here, $\lambda$ is a so-called Lagrange parameter, which turns out to be the pressure $\Delta p$ in the liquid. $G[A]$ is the Gibbs free energy functional of the system. In addition to surface energies, we want to include gravitational body forces as well. The energy density of the gravitational energy is $\rho g z$. Hence, the total functional that we aim to minimize is

$$\begin{aligned} G[A] = E_{surf}[A] + E_g[A] - \Delta p V = \int \gamma dA_{lv} + \int (\gamma_{sl} - \gamma_{sv}) dA_{sl} \\ + \int (\rho g z - \Delta p) dV \end{aligned} \tag{1.30}$$

We assume that the solid–liquid interface is flat and choose to make it coincide with the $(x, y)$-plane of our coordinate system. To proceed, we rewrite the first and the last integral in Eq. (1.30) as integrals over the drop–substrate interfacial area $A_{sl}$ like the second one. Furthermore, we rewrite the integrand as a function of $h(x, y)$ and $h'(x, y)$, our explicit parameterization of the drop shape. To do so, we note that $dA_{lv} = (1 + (\partial_x h)^2 + (\partial_y h)^2)^{1/2} dx\, dy$ and $dA_{sl} = dx\, dy$. Furthermore, we can write $dV = dx\, dy\, dz$ in the third integral and carry out the $z$-integration from 0 to $h(x, y)$. Using these expressions, we find

$$\begin{aligned} G[h(xy), \partial_x h, \partial_y h] = \iint_{A_{sl}} dx\, dy \\ \left\{ \gamma \sqrt{1 + (\partial_x h)^2 + (\partial_y h)^2} + \gamma_{sl} - \gamma_{sv} + \frac{1}{2} \rho g \, h^2 - \Delta p \, h \right\} \end{aligned} \tag{1.31}$$

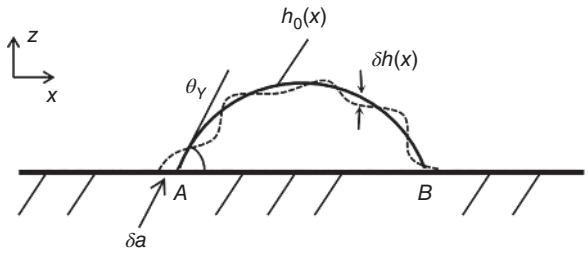


**Figure 1.14** Illustration of a sessile drop with equilibrium surface profile $h_0(x)$ and arbitrary variation $\delta h(x)$.

To minimize notational effort, we will restrict ourselves in the following to a two-dimensional problem such that the interface position is a function of one spatial coordinate $x$ only as sketched in Figure 1.14.

In this case, the integration domain on the substrate extends from the left contact line position at $x = A$ to the right one at $x = B$. The surface profile is given by a function $h(x)$. Dropping all $y$-dependencies and writing $h' = \partial_x h$, the variation of Eq. (1.31) becomes

$$\delta G = \delta \int_A^B \left[\gamma\sqrt{1+h'^2} + \gamma_{sl} - \gamma_{sv} + \frac{1}{2}\rho g h^2 - \Delta p\, h\right] dx = 0 \tag{1.32}$$

To carry out the variational minimization, we write $h(x) = h_0(x) + \delta h(x) = h_0(x) + \alpha\eta(x)$, where $h_0(x)$ is the equilibrium shape that we seek and $\eta(x)$ is an arbitrary variation around that equilibrium. $\alpha$ is a small parameter. We denote the integrand of Eq. (1.32) as $\tilde{g}(h, h')$. The variational derivative then reads

$$\delta G = \delta b\, \tilde{g}(B) - \delta a\, \tilde{g}(A) + \int_A^B \left[\frac{\partial \tilde{g}}{\partial h}\frac{\partial h}{\partial \alpha}d\alpha + \frac{\partial \tilde{g}}{\partial h'}\frac{\partial h'}{\partial \alpha}d\alpha\right] dx \tag{1.33}$$

where the first two terms arise from the variations $\delta a$ and $\delta b$ of the contact line positions. The integral can be further simplified by partial integration of the second term

$$\int_A^B \frac{\partial \tilde{g}}{\partial h'}\frac{\partial h'}{\partial \alpha}d\alpha dx = \frac{\partial \tilde{g}}{\partial h'}\frac{\partial h}{\partial \alpha}d\alpha\Big|_A^B - \int_A^B \frac{d}{dx}\left(\frac{\partial \tilde{g}}{\partial h'}\right)\frac{\partial h}{\partial \alpha}d\alpha dx \tag{1.34}$$

Inserting into Eq. (1.33) we find

$$\delta G = \delta b\, \tilde{g}(B) - \delta a\, \tilde{g}(A) + \frac{\partial \tilde{g}}{\partial h'}\delta h\Big|_A^B + \int_A^B \left(\frac{\partial \tilde{g}}{\partial h} - \frac{d}{dx}\left(\frac{\partial \tilde{g}}{\partial h'}\right)\right)\delta h dx \tag{1.35}$$

Here, the variations of the contact line positions $\delta a$ and $\delta b$ are not independent of the variation of $\delta h(A)$ and $\delta h(B)$. Rather, we have $\delta h(A) = -h'(A)\,\delta a$ and $\delta h(B) = -h'(B)\delta b$ by geometry. Inserting this yields

$$\begin{aligned}\delta G = {} & \delta b\left(\tilde{g}(B) - \frac{\partial \tilde{g}}{\partial h'}h'\right) - \delta a\left(\tilde{g}(A) - \frac{\partial \tilde{g}}{\partial h'}h'\right) \\ & + \int_A^B \left(\frac{\partial \tilde{g}}{\partial h} - \frac{d}{dx}\left(\frac{\partial \tilde{g}}{\partial h'}\right)\right)\delta h(x) dx = 0\end{aligned} \tag{1.36}$$

Since $\delta G$ has to vanish for arbitrary variations $\delta h$, $\delta a$, and $\delta b$, all the expressions in the parentheses in Eq. (1.36) must vanish independently. The expression under

the integral in the third term is the Euler–Lagrange equation for the $\tilde{g}(h, h')$. Inserting the definition for $\tilde{g}$ from Eq. (1.32) yields

$$\gamma\, \kappa(x) = \Delta p - \rho\, g\, h(x)$$

where we used $\kappa = -h'' / (1 + h'^2)^{3/2}$ to take into account the proper sign convention for the radius of curvature. Hence, we recover the Young–Laplace equation including the gravitational term as the Euler–Lagrange equation of our minimization procedure. Inserting the definition of $\tilde{g}$ into the conditions that arise from the variations $\delta a$ and $\delta b$, and taking into account $\tilde{g}(x_A) = \gamma(1 + h'(x_A)^2)^{1/2} = \gamma / \cos\theta$, we recover Young's equation, Eq. (1.17). As we already mentioned in our heuristic considerations in Section 1.4, we thus find from the general formalism of variational energy minimization that gravity does indeed *not* affect the contact angle – only the shape of the drop away from the contact line.

In summary, we have now seen how both basic equations of capillarity arise from one calculation based on the general principle of energy minimization. Note that the procedure to include the gravitational body force as an energy density in Eq. (1.30) is rather general. The same strategy can be applied to include molecular interaction forces in thin films (see Section 1.6) as well as the electrostatic body forces that are responsible for EW and dielectrophoresis.

## 1.6 Wetting at the Nanoscale

So far, we considered wetting problems from a macroscopic perspective. However, we know from our brief discussion in Section 1.1 that interfacial tensions arise from molecular interaction forces and that these forces typically have a range of a few molecular diameters. Therefore, the question arises, how these molecular forces affect the wetting behavior on scales that are comparable to the range of the interaction forces. From an applied perspective, this question may seem somewhat academic at first glance since drop dimensions of interest are typically much larger. Yet, nanoscale wetting properties are important for the macroscopic behavior of drops for several reasons: First of all, liquids with a finite vapor pressure tend to adsorb from the vapor phase onto solid surfaces. In daily life, this leads to the formation of molecularly thin films of water on almost any surface. Depending on the ambient humidity and the nature of the molecular interaction forces (hydrophilicity/hydrophobicity of the surface), these films can become several nanometers thick. Since sessile drops of liquid generate their own atmosphere of saturated vapor around them, the solid surface next to a partially wetting drop is in general also covered by such a thin film, as sketched in the inset of Figure 1.15. Conceptually, this is quite a dramatic observation by itself: An equilibrated solid–vapor interface is not the same as a perfectly dry solid–vacuum interface. Similarly, the equilibrium solid–vapor interfacial tension $\gamma_{sv}$ is *not* the same as the solid–vacuum interfacial tension: The spontaneous adsorption of the thin film always reduces the interfacial tension. In practice, the presence or absence of such films can also have important macroscopic consequences, e.g. for the friction and lubrication of solid surfaces and for electrostatic

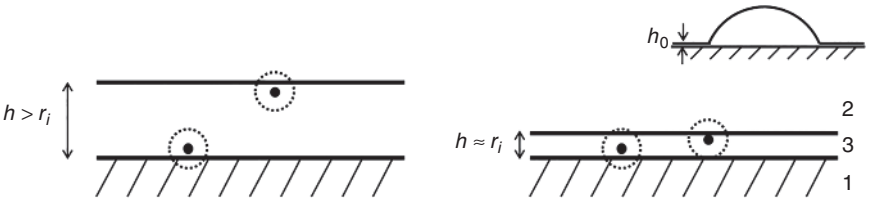


**Figure 1.15** Relevance of molecular interaction forces for the surface energy of thin liquid films. Illustration of necessity of a correction term for $h \approx r_i$. The numbers on the far right indicate the media 1 (solid), 2 (ambient), and 3 (film). Inset: illustration of a partially wetting drop accompanied by molecularly thin wetting films.

charging of surfaces, which is a key concern when handling sensitive electronic devices in dry environments. In fact, it turns out that the existence of such thin films is not limited to volatile liquids. Even drops of partially wetting nonvolatile fluids are usually surrounded by such films if given enough time to equilibrate. Their thickness $h_0$ is particularly large if one of two liquid phases wets a solid much better than the other. A typical example is oils used as ambient medium in EW devices that wet hydrophobic polymer surfaces much better than water.

### 1.6.1 The Effective Interface Potential

To develop a quantitative description of the thin wetting films, we consider the free energy of a solid surface covered by a liquid film with a homogeneous thickness $h$. If $h$ is large compared with the range $r_i$ of the molecular interaction forces, the solid–liquid interface and the liquid–vapor interface are both well defined and separated from each other, as illustrated on the left of Figure 1.15. The free energy per unit area is then simply given by the sum of the interfacial energies of the solid–liquid and the liquid–vapor interface, i.e. $G \equiv \gamma_{sl} + \gamma$ independent of the exact value of $h$. If $h \approx r_i$, however, both interfaces are within the range of interactions of the molecules in the film. Hence, there are no longer two separate interfaces. There is only one composite interface that includes the thin liquid film. A very convenient manner to describe this situation is to introduce a new quantity, the so-called effective interface potential $\Phi(h)$. $\Phi$ is an excess quantity that takes into account all necessary corrections due to the molecular forces with respect to the reference state of two separate interfaces. Before discussing an explicit expression for $\Phi$ in terms of some specific molecular interaction force, let us use this general definition to re-express the thickness-dependent free energy of the interface as

$$G(h) = \gamma_{sl} + \gamma + \Phi(h) \tag{1.37}$$

We can readily infer a few necessary properties of $\Phi(h)$ from the limiting cases without knowing any details about the specific type of molecular interactions. First, the absolute value of $\Phi$ should be of the same order of magnitude as the interfacial tensions, because both have the same physical origin. Since the effect of molecular interactions vanishes for $h > r_i$, we know that $\Phi(h) \to 0$ for $h \gg r_i$. Furthermore, we know that $G(h) \to \gamma_{sv}$ for $h \to h_0$. (Note that we include the thin

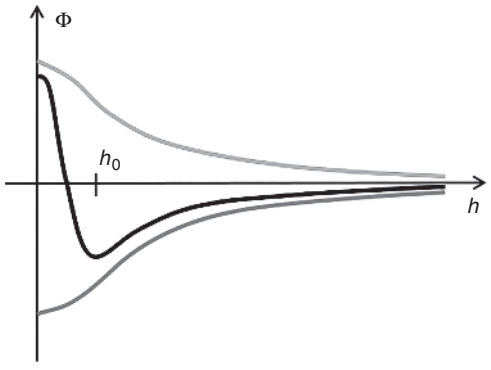


**Figure 1.16** Effective interface potential versus film thickness for generic cases of complete wetting (top), pseudopartial wetting (middle), and partial wetting (bottom).

liquid film explicitly in the definition of $\gamma_{sv}$.) Comparing Eqs. (1.12) and (1.37), we find $\Phi(h_0) = S$. For complete wetting systems, where the spreading parameter $S$ is positive, $\Phi$ is typically a function that decays monotonically from $\gamma_{sv}$ to zero within the range $h = 0, \ldots, r_i$; see top curve in Figure 1.16. This shape of $\Phi(h)$ implies that reducing $h$ to values of the order of $r_i$ or less increases the surface energy of the system and is thus unfavorable. The minimum of the interfacial energy corresponds to an *infinitely* thick liquid film – exactly as expected for a completely wetting system. (*Infinite* in this context means $\gg r_i$.) This explains the name *effective interface potential*: $\Phi(h)$ is the interaction potential per unit area between the solid–liquid and the liquid–vapor interface. Correspondingly, we can define a pressure, the so-called disjoining pressure $\Pi(h)$, as the negative gradient of the potential

$$\Pi(h) = -\frac{d\Phi}{dh} \tag{1.38}$$

For partial wetting systems we know that $S = \Phi(h_0) < 0$. This means that the system gains energy by reducing the film thickness once it comes within the range of the interface potential. In partial wetting conditions, the interfacial tensions are related to the contact angle by Young's equation. Eliminating $\gamma_{sl}$ and $\gamma_{sv}$, we find

$$\Phi(h_0) = S = \gamma(\cos\theta_Y - 1) \quad \text{(for partial wetting)} \tag{1.39}$$

This is a remarkable equation. It states that Young's angle is completely determined by the value of the minimum of $\Phi(h)$. The actual functional form of $\Phi$ is irrelevant for the macroscopic angle that is observed in conventional contact angle goniometry measurements. The middle and the bottom curves in Figure 1.16 both show examples of interface potentials for partially wetting systems. The bottom curve shows a pure partial wetting case, for which the thickness of the equilibrium film strictly vanishes. The middle curve illustrates the more common case with a finite value of $h_0$. Sometimes, this regime is denoted as *pseudopartial* wetting. It is characterized by a combination of an attractive molecular interaction force at long distances and a sharply increasing repulsive contribution at short distance. This short-range part of the effective interface potential is typically related to the same short-range chemical forces as the repulsive part of the molecular interaction potential shown in Figure 1.1c.

### 1.6.2 Case Studies

#### 1.6.2.1 The Effective Interface Potential for van der Waals Interaction

We already inferred quite a few general properties of the effective interface potential without specifying the microscopic molecular interactions. Nevertheless it is very instructive to derive a quantitative expression for $\Phi(h)$ for a specific type of molecular interaction. We will choose van der Waals interactions as an example because of their ubiquity and because they give rise to a simple functional form of $\Phi$. (The case of screened Coulomb interactions, which is important for the electrolytes typically used in EW, will be addressed separately in Chapter 4.) Fundamentally, van der Waals interaction arises from quantum mechanical fluctuations of the electron cloud of molecules that give rise to fluctuating dipole moments. These fluctuating dipole moments generate electric fields that polarize other molecules. In the end, this leads to an interaction that is always attractive between two isolated atoms or molecules and that decays as function of the distance $r$ with $r^{-6}$. This gives rise to the attractive part of the molecular interaction potential in Figure 1.1. To first approximation, the van der Waals interaction energy of a system of many interaction molecules can be considered as pairwise additive. Hence, if we want to know the interaction energy of a liquid film of a certain thickness $h$ covering a solid substrate, we need to add the van der Waals interaction energy of each molecule in the liquid with each molecule in the substrate and with the rest of the adsorbed liquid film. Details of this calculation as well as a discussion of the more advanced quantum mechanical derivations of the van der Waals interaction can be found in References [2, 3]. For a system consisting of a substrate (medium 1) interacting through a thin film (medium 3) with a second immiscible phase (ambient air, oil, etc.; medium 2) with parallel interfaces, as shown on the RHS of Figure 1.15, the resulting effective interface potential is

$$\Phi(h) = \frac{A_H}{12\pi h^2} \tag{1.40}$$

The corresponding disjoining pressure is given by

$$\Pi(h) = -\frac{d\Phi}{dh} = \frac{A_H}{6\pi h^3} \tag{1.41}$$

Here, $A_H$ is the so-called Hamaker constant. It is characteristic for the specific three-phase system. Note that $\Phi$ decays rather slowly as $h^{-2}$ with increasing film thickness, much slower than the $r^{-6}$-dependence of the underlying molecular interaction potential suggests. This weaker exponent arises from the summation over all the interacting pairs of molecules in the substrate and in the thin film. This makes van der Waals interaction a *long-range* force in the terminology of wetting science. Still, *long range* typically means no more than several nanometers.

The complete theory of van der Waals interaction has been worked out by Lifshitz using a quantum mechanical analysis that takes into account the response of the materials to electromagnetic fields integrated over all possible frequencies. The result is that the Hamaker constant $A_H = A_{132}$ for three materials interacting

with each other can be written as

$$A_{132} = -C_1 \frac{\varepsilon_1 - \varepsilon_3}{\varepsilon_1 + \varepsilon_3} \frac{\varepsilon_2 - \varepsilon_3}{\varepsilon_2 + \varepsilon_3} - C_2 \frac{(n_1^2 - n_3^2)(n_2^2 - n_3^2)}{\sqrt{n_1^2 + n_3^2}\sqrt{n_2^2 + n_3^2}(\sqrt{n_1^2 + n_3^2} + \sqrt{n_2^2 + n_3^2})} \tag{1.42}$$

Here, $C_1 = \frac{3k_BT}{4} \approx 3.5 \times 10^{-21}$ J and $C_2 = 3\hbar\omega/16\sqrt{2} \approx 1.40 \times 10^{-20}$ J, where $\hbar$ is Planck's constant and $\omega \approx 10^{15}\,\mathrm{s}^{-1}$ is a typical optical frequency. (We choose the sign of $A_{132}$ here consistent with the wetting literature; see, e.g. [1], which is opposite to [2, 3].) The order of the subscripts in $A_{123}$ indicates that medium 1 interacts with medium 2 through the ambient medium 3 according to the conventional notation. The first term in Eq. (1.42) involves the static polarizability of the materials quantified in terms of the dielectric permeabilities $\varepsilon_i$ ($i = 1, 2, 3$). The second term describes the response at optical frequencies and is expressed in terms of the refractive indices $n_i$. Upon inserting numbers, one finds that the high frequency optical term involving the refractive indices usually dominates. Exceptions occur in case of index matching, i.e. when the refractive index of the ambient medium 3 equals the refractive index of one of the two other materials. In that case, the high frequency part obviously vanishes. Furthermore, Eq. (1.42) also shows that nature *likes* to arrange phases in the order of their polarizabilities. That is, complete wetting with $A_{132} > 0$ is found for $n_1 > n_2 > n_3$ or $r\, n_1 < n_2 < n_3$ (and analogue for the low frequency permittivities). Vice versa, if medium 3 has either the highest or the lowest polarizability, the system displays partial wetting with $A_{132} < 0$. In this case, a film of medium 3 on the substrate is unstable and transforms into a drop with a finite contact angle. That is, medium 3 is expelled from the space in between mediums 1 and 2 (except for a possible thin film that is stabilized by a short-range chemical force).

In EW experiments, the substrates are frequently made of fluoropolymers such as Teflon AF with a very low refractive index $n_1 = 1.31$ in the visible range and a dielectric constant of $\varepsilon_1 = 1.93$. If we perform an experiment with aqueous drops in ambient oil, the water is medium 2 with a refractive index of $n_2 = 1.33$ and a very large dielectric constant of $\varepsilon_2 = 81$. Typical alkane or silicone oils have a refractive index of $n_3 = 1.4$–$1.45$ and a dielectric constant of $\varepsilon_3 = 2$–$3$. These values imply that the optical contribution favors partial wetting, whereas the static contribution favors complete wetting. Due to the large value of the dielectric constant of water, the balance is actually very subtle. Using $\varepsilon_3 = 2$ and $n_3 = 1.43$ (hexadecane) yields a value of $A_{132} = -2.7 \times 10^{-23}$ J. That is, the system is expected to display partial oil wetting, albeit with a rather small value of the Hamaker constant. Using $\varepsilon_3 = 2.5$ and $n_3 = 1.4$ (for some specific silicone oils) yields a value of $A_{132} = +3.8 \times 10^{-22}$ J. That is, the system is expected to display complete oil wetting and thus a stable oil film in between the water drop and the underlying fluoropolymer substrate. While additional molecular interactions may modify the details of the picture, the calculation shows that a proper choice of materials has important consequences for the microscopic wetting behavior that can affect the outcome of experiments – and the reliability of devices.

#### 1.6.2.2 Equilibrium Surface Profile Near the Three-Phase Contact Line

The disjoining pressure appears as an additional contribution in the Young–Laplace equation if the thickness of a liquid film is of the order $r_i$. For a two-dimensional system, the corrected form of the equation reads

$$\gamma \frac{h''}{(1+h'^2)^{3/2}} = \frac{d\Phi}{dh} - \Delta p \tag{1.43}$$

Equation (1.43) can be derived formally by variational minimization of the Gibbs free energy in analogy with our calculation for gravity as an external force in Section 1.5. Replacing the latter by the contribution due to the interface potential, we can rewrite Eq. (1.31) in two dimensions as

$$G[h, h'] = \int dx \, \{\gamma \sqrt{1+h'^2} + \gamma_{sl} - \gamma_{sv} + \Phi(h)\} \tag{1.44}$$

Functional minimization of this expression along the lines of Section 1.5 leads to Eq. (1.43). (Note that we can set $\Delta p = 0$ because the surface of the macroscopic drop is local flat on the very small scale that is affected by the molecular forces.) Hence, the thickness profile of molecularly thin films is governed by the balance of capillary pressure and disjoining pressure alone.

This has major consequences for the local surface profile: Far away from the contact line, the disjoining pressure is negligible. Hence, the liquid surface is flat, and the balance of all interfacial tensions acting on the gray-shaded control volume in Figure 1.17 yields Young's angle as a macroscopic contact angle. Note that we included explicitly the molecularly thin wetting film with a finite thickness $h_0$ corresponding to a *pseudopartial wetting* condition. Within the range of the molecular interactions, $\Phi$ is non-negligible, and the disjoining pressure distorts the surface profile $h(x)$, leading a position-dependent local slope angle $\phi(x)$. Very much like the case of a drop in the presence of gravity, we can obtain this profile by integrating Eq. (1.43). We find

$$\cos \phi(x) = \cos \theta_Y - \frac{\Phi(h(x))}{\gamma} \tag{1.45}$$

Since $\cos \phi(x) = 1/\sqrt{1+h'^2}$, Eq. (1.45) is still a first-order differential equation for $h(x)$. Yet, we can already read from the equation that positive values of $\Phi(h)$ give rise to local slope angles $\phi > \theta_Y$ and vice versa. Because of the short range of the molecular interaction forces, such disjoining pressure-induced deformations

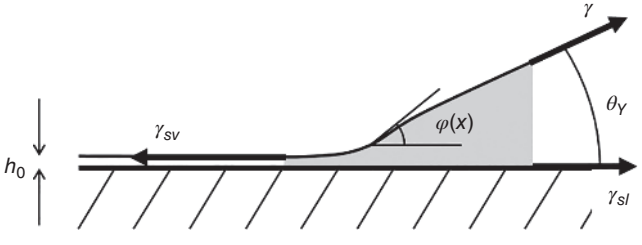


**Figure 1.17** Profile of a liquid surface in the vicinity of a three-phase contact line. Note that $\gamma_{sv}$ includes the contribution from the thin film, i.e. $\gamma_{sv} = \gamma + \gamma_{sl} + \Phi(h_0)$.

of liquid surfaces are extremely difficult to observe. As mentioned above, optical imaging of drops does not allow to access these scales and therefore always shows Young's angle. In Chapter 5, we will use a very similar approach as discussed here to calculate the surface profile in the vicinity of the contact line in EW. In that case, electrical stresses will take over the role of the disjoining pressure. In contrast to the molecular interaction forces, the electrostatic forces have a much larger range. Therefore, deformations of the surface due to local electric fields close to the contact line can be visualized optically for suitable conditions.

## 1.7 Wetting of Heterogeneous Surfaces

All our considerations so far dealt with perfectly homogeneous and flat surfaces. The contact angle and the drop shape were completely determined by the interfacial tensions of the three phases and the desire of the system to minimize its free energy in equilibrium. In contrast to this idealized situation, real surfaces are never perfectly flat and homogeneous. They display heterogeneity, usually of both topographic and chemical nature. Such heterogeneities occur on various length scales with defect sizes ranging from atomic to macroscopic dimensions. Wetting on real surfaces is always wetting of heterogeneous surfaces. If we are interested in the wetting behavior of drops of some finite size, it is useful to distinguish between heterogeneity on scales that are either much smaller than the drop size or comparable to it. Small-scale heterogeneities are unavoidable. They give rise to usually invisible microscopic deformations of the drop along the three-phase contact line. Their most important macroscopic consequence is contact angle hysteresis. Large-scale heterogeneity gives rise to macroscopically visible deformations of the drops. In a technological context, macroscopic heterogeneities are frequently imprinted onto the surface to achieve certain properties. Examples include superhydrophobicity caused by small-scale heterogeneity as well as EW-based lab-on-a-chip devices, in which actively switchable large-scale heterogeneity is used to deform and transport drops. In this section, we will analyze the physical principles governing the wetting of heterogeneous surfaces in static conditions. Most basic aspects will be established for two-dimensional systems. Toward the end of the chapter, we address contributions arising from deformations of the liquid surface in three dimensions.

### 1.7.1 Young–Laplace and Young–Dupré Equation for Heterogeneous Surfaces

The first question to wonder is whether the basic laws of capillarity still apply for heterogeneous surfaces. Let us consider a sessile drop on a heterogeneous surface in two dimensions, as sketched in Figure 1.18. The free energy of the drop is formally given by a similar integral as before:

$$G = \int ds_x [\gamma \sqrt{1 + (\partial_x h)^2} + \gamma_{sl}(x) - \gamma_{sv}(x) - \Delta p\, h] \tag{1.46}$$

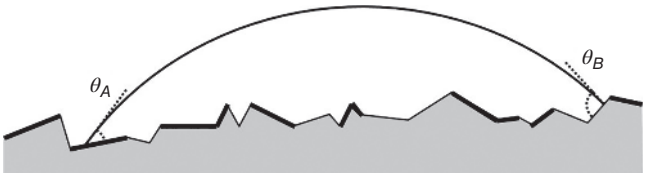


**Figure 1.18** Sessile drop on topographically and chemically heterogeneous surface (bold lines on surface: material *A* – small contact angle $\theta_A$; thin lines: material *B* with $\theta_B > \theta_A$).

Compared with Eq. (1.31), there are two differences caused by the topographic roughness and the chemical heterogeneity, respectively: First, the integral extends along the contour of the actual rough solid–liquid interface (denoted as $ds_x$) rather than simply along $x$. Following all the ups and downs on the rough surfaces gives rise to an enhancement of the true solid–liquid interfacial area as compared with the projected area. Second, the chemical heterogeneity is reflected in position-dependent values $\gamma_{sl}(x)$ and $\gamma_{sv}$(x).

Variational minimization of Eq. (1.46) along the formalism described in Section 1.5 shows that the Laplace equation remains unaffected by the surface heterogeneity, i.e. the pressure drop across the liquid surface is still given by $\Delta P_L = \gamma\kappa$. This should not surprise us. The drop surface itself is not directly affected by the presence of the heterogeneity on the substrate surface. The influence is only indirect, via the boundary condition at the solid–liquid interface. Hence, it is Young's equation that is affected by the presence of heterogeneity. And even for Young's equation, the modification is – in some sense – minor: If the contact line is located somewhere within a locally homogeneous region on the surface, i.e. away from boundaries between patches of different chemical composition or surface orientation, the principle of the local variation of the contact line position still holds. Hence, Young's equation simply applies locally with the position-dependent local Young angle $\theta_Y(x)$ according to the local composition and orientation of the surface, i.e. $\cos\theta_Y(x) = (\gamma_{sv}(x) - \gamma_{sl}(x))/\gamma$. As illustrated in Figure 1.18, the local contact angle $\theta_Y(x)$ is to be measured relative to the local orientation of the surface.

The range of the molecular interactions provides a good estimate for the minimum size of patches of well-defined local properties. If two types of atoms *A* and *B* with different interaction potentials are arranged on a surface in patches with a size of a few times the molecular interaction range, well-defined *A* and *B* regions arise (Figure 1.19a). On these patches, local contact angles $\theta_A$ and $\theta_B$ assume the same values as on macroscopic homogeneous surfaces. In contrast, placing *A* and *B* atoms next to each other in an alternating fashion produces an energetically more or less homogeneous surface with mixed properties. While the observation of surface heterogeneity is in practice often limited by the resolution of the


**Figure 1.19** Schematic of a surface consisting of two different types of molecules *A* and *B* patched in groups of 5 (a) and alternating (b).

instruments that are used to characterize the surfaces, the range of the molecular interactions provides a fundamental lower limit.

The existence of chemical domains with surface areas of a few nanometers raises another important problem: Since the balance of surface energies on a lyophobic (*liquid-repelling*) patch is less favorable for wetting, such a patch represents an energy barrier for the spreading liquid. The height of such an energy barrier is of the order of $\Delta E \approx \gamma\, \Delta \cos\theta_Y \cdot l^2$, where $l$ is the size of the patch. For $l = 5$ nm and a typical wettability contrast $\gamma \Delta\cos\theta = 0.01$ J/m$^{-2}$, we find $\Delta E \approx 2.5 \times 10^{-19}$ J. This value is much larger than the thermal energy at room temperature, which is $k_B T \approx 4 \times 10^{-21}$ J. Hence, the contact line is unable to overcome such a wetting defect by thermal activation. As a consequence, it gets trapped in some metastable nonequilibrium position: The drop is unable to explore the surface to reach the energetically most favorable configuration. The existence of a large number of such metastable states is characteristic for the wetting on heterogeneous surfaces. As in many other fields of physics, the existence of metastable states implies hysteresis and history dependence of the actual configuration of the system. This is arguably the most important physical consequence of surface heterogeneity.

### 1.7.2 Gibbs Criterion for Contact Line Pinning at Domain Boundaries

On surfaces with sufficiently large patches (i.e. $l \geq$ several nm) of well-defined chemical composition and orientation, the contact angle on each patch is well defined, as illustrated in Figure 1.20. If the contact line is located at the boundary between two adjacent domains, however, this is no longer true. In this case, it is not clear whether the more lyophilic or the more lyophobic angle should be chosen for a surface with chemical patches $A$ and $B$. Similarly, for a topographically patterned surface, it is not clear with respect to which *facet* of the surface the contact angle should be measured.

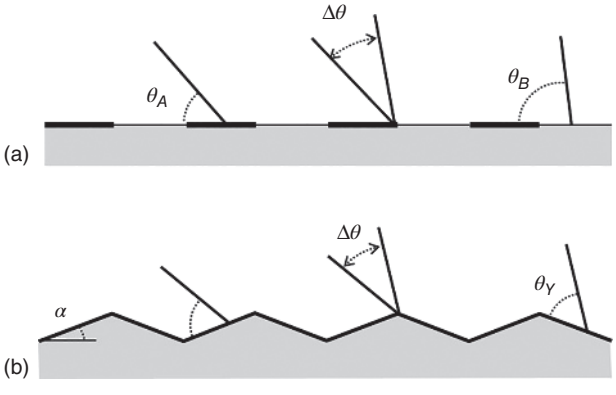


**Figure 1.20** Local contact angle on heterogeneous surfaces and Gibbs pinning at domain boundaries for chemically heterogeneous flat surfaces ((a); thick lines, philic regions; thin lines, phobic regions) and chemically homogeneous rough surfaces (b).

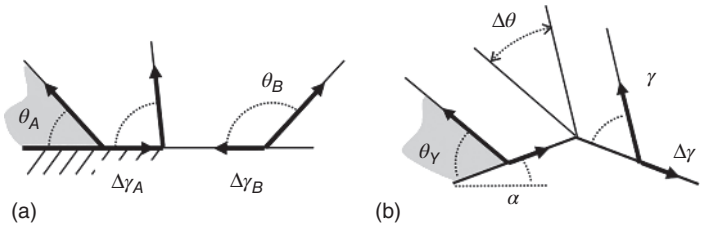


**Figure 1.21** Force balance for a contact line upon approaching a domain boundaries for chemical heterogeneity (a) and a topographic corner (b).

We gain some more physical insight if we consider the local force balance as a contact line is approaching an $A$–$B$ domain boundary as illustrated in Figure 1.21a. Let us assume $\theta_A < 90^\circ$ and $\theta_B > 90^\circ$. When the contact line is on the more lyophilic side of the boundary, the contact angle is $\theta_A$ such that the projection of the surface tension $\gamma \cos\theta_A$ balances the net force $\Delta\gamma_A = \gamma_{sv}^A - \gamma_{sl}^A$ exerted on the liquid by the solid substrate. $\Delta\gamma_A$ is thus pointing toward the right, i.e. toward the domain boundary. Conversely, if the contact line is on the more lyophobic side of the boundary, the corresponding force $\Delta\gamma_B$ exerted by the substrate points toward left – i.e. again toward the domain boundary. In equilibrium this force is of course balanced by the liquid assuming a contact angle $\theta_B$. If the contact line is exactly at domain boundary, it will experience a force toward pushing it toward the domain boundary for any contact angle $\theta$ satisfying

$$\theta_A < \theta < \theta_B \tag{1.47}$$

Any slight perturbation that tries to move the contact line away from the domain boundary is restored by the surface tension force. Hence, the contact line is stably *pinned* to the domain boundary for any value of $\theta$ within this interval. Note that this reasoning only holds for domain boundaries where the liquid occupies the more lyophilic side of the domain boundary. The same reasoning for the opposite situation where the liquid occupies the more lyophobic side of the boundary shows that this configuration is unstable and the contact line is always driven away from the boundary. The analogue reasoning for a topographically patterned substrate with well-defined inclination angles leads to pinned configurations at the tops of the pattern for contact angles with the respect to the horizontal within the range

$$\theta_Y - \alpha < \theta < \theta_Y + \alpha \tag{1.48}$$

as illustrated in Figure 1.21b. Equations (1.47) and (1.48) are generally known as Gibbs criterion for contact line pinning at domain boundaries.

### 1.7.3 From Discrete Morphology Transitions to Contact Angle Hysteresis

The consequences of Gibbs pinning for the morphologies of drops on heterogeneous surfaces and for the occurrence of contact angle hysteresis were investigated in great detail in the 1960s and 1970s for macroscopically patterned surface,

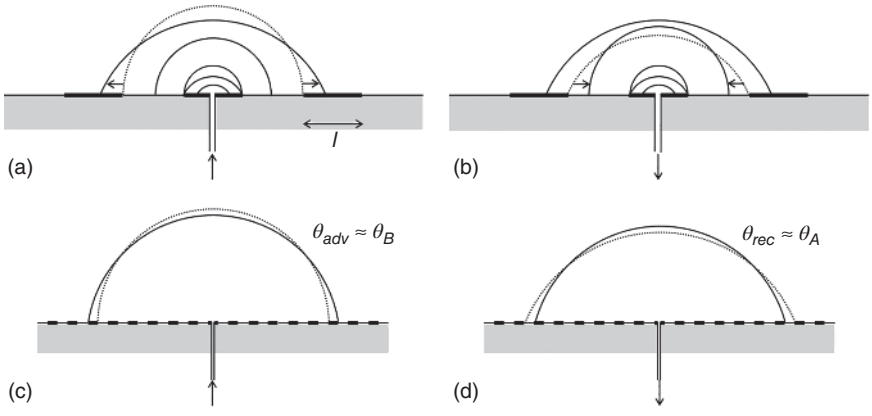


**Figure 1.22** Evolution of the drop shape upon increasing and decreasing the drop volume on a surface with alternating lyophilic ($\theta_A$) and lyophobic ($\theta_B$) domains of width $l$. (a) and (b) for drop size $R \approx l$, (c) and (d) for $R \gg l$.

e.g. in seminar contributions by Johnson and Dettre [10] and Huh and coworkers [11].

Let us consider a drop on a surface with alternating lyophilic and lyophobic stripes. The drop is gradually inflated and deflated by pumping liquid in and out through a hole in the substrate in the center of a lyophilic domain, as sketched in Figure 1.22. For very small volumes $V$ the drop only wets the central lyophilic domain (smallest drop in Figure 1.22a). The contact angle $\theta = \theta_A$ is constant as the volume and the drop radius increase as shown in Figure 1.23. The drop spreads until the contact line reaches the first domain boundary with the lyophobic domains at $V = V_1$. At that moment, the contact line gets pinned. Subsequently, the drop accommodates the increasing volume by increasing its contact angle until $\theta$ reaches the contact angle $\theta_B$ of the lyophobic domain for $V = V_2$. At that moment, the contact line gets depinned, and the drop spreads further at constant $\theta = \theta_B$ until it reaches the next domain boundary at $V = V_3$. Since the contact line reaches that boundary from the lyophobic side, it is unstable and experiences at force pulling it onto the next lyophilic domain. This gives rise to an abrupt transition from the shape indicated by the dotted line in Figure 1.22a with $\theta = \theta_B$ to the outermost one drawn as solid arc with $\theta = \theta_A$. Simultaneously, $r_{sl}$ increases by some geometry-dependent amount that is dictated by volume conservation.

If we reverse the pumping direction, the contact line recedes again, and the drop shrinks at constant $\theta = \theta_A$. As the contact line reaches the lyophilic–lyophobic domain (dotted circle in Figure 1.22b), it becomes unstable again. Another abrupt transition in the morphology of the drop occurs in this case toward a small drop radius with $\theta = \theta_B$, as indicated by the arrows. From there on, the shrinking drop volume can be accommodated again by reducing the drop diameter on the lyophobic domain at constant $\theta = \theta_B$ until the next boundary with the innermost lyophilic domain is reached. There, the contact line gets pinned in a stable configuration until $\theta$ has decreased down to $\theta_A$. From that moment on, the drop only wets the inner lyophilic domain and shrinks again

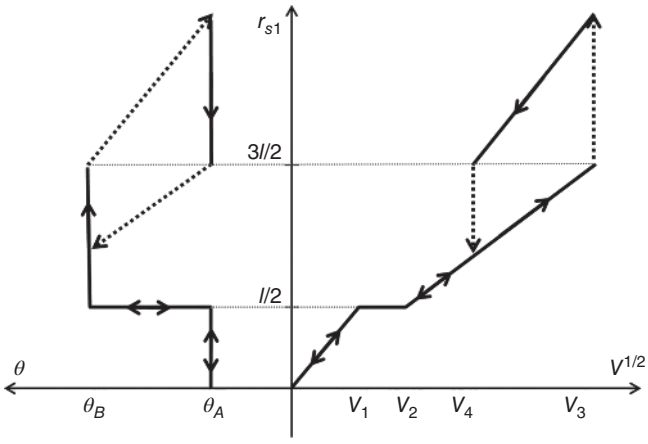


**Figure 1.23** Contact angle and drop base radius versus square root of the drop volume (in two dimensions).

with constant $\theta = \theta_A$. For volumes $V_3 > V > V_4$, there are thus two mechanically stable drop morphologies with different drop radius and contact angle. The actually realized morphology depends on the history of the drop. Upon cycling the volume up and down, the drop follows a hysteresis loop. We denote the abrupt transition between two distinct drop shapes wetting a different number of stripes as a morphology transition. Morphology transitions take place whenever a variation of a control parameter, i.e. the drop volume in the present example, renders the initial morphology unstable. In the present case this happens due to a violation of the Gibbs pinning criterion.

So far, we discussed a situation in which the stripe width, i.e. the characteristic length scale of the heterogeneity, is a sizeable fraction of the drop radius. In this case, a morphology transition affects the drop shape on a global scale. If we repeat our reasoning for $l \ll r_{sl}$, the scenario sketched above still holds. Yet, there is one important difference: The increase in $r_{sl}$ required to decrease the contact angle from $\theta_B$ to $\theta_A$ is now larger than $l$. Since $\theta$ is a monotonously decreasing function of $r_{sl}$, however, the jumping contact line becomes trapped again at the next lyophobic domain boundary, while $\theta$ has only decreased by a small amount, as illustrated in Figure 1.22c. In the limit of microscopic roughness with $l/r_{sl} \to 0$, the amount of contact angle relaxation per transition becomes negligible. As a consequence, we observed a constant *advancing* contact angle $\theta_a$ while the drop volume is increased. For the two-dimensional system of alternating stripes, this advancing contact angle is given by the contact angle of the lyophobic domain, i.e. $\theta_a = \theta_B$. The analogue reasoning for decreasing drop volumes shows that the contact angle of the then *receding* contact line also assumes a constant value, the receding contact angle $\theta_r$, which is given by the contact angle $\theta_A$ of the lyophilic domain. Depending on whether the contact line advances or recedes, we thus observe $\theta_a$ or $\theta_r$. A sessile drop, for which the contact line is neither advancing nor receding $\theta$, can assume any value between $\theta_a$ and $\theta_r$, depending on the history. The difference between advancing and receding contact angle is the contact angle

hysteresis $\Delta\theta = \theta_a - \theta_r = \theta_B - \theta_A$. This equation also implies that. $\Delta\theta$ is a direct measure of the degree of heterogeneity of the surface.

The simple example of a model heterogeneity of alternating lyophilic and lyophobic stripes thus illustrates two important general aspects of wetting of heterogeneous substrates: First, it shows how surface heterogeneity gives rise to competing metastable drop configurations. Second, it illustrates that the existence of these metastable drop configurations causes both macroscopic morphology transitions between different drop shapes and contact angle hysteresis. The difference between global morphology transitions and local relaxations of the contact line is not a fundamental one, but rather of practical nature related to the resolution at which we investigate the system. The principle of destabilization due to a local violation of Gibbs pinning criterion (see Figure 1.21) is the same in both cases.

The specific type of surface heterogeneity is obviously idealized. For instance, we assumed infinitely sharp transitions between adjacent domains of low and high contact angle. In practice, the boundaries between adjacent domains will always be smeared out to some degree. As discussed in the context of Figure 1.19, the finite range of the molecular interaction forces always gives rise to some degree of smoothing even for atomically sharp domain boundaries. The continuous character of domain boundaries (or topographic corners) introduces two new aspects. On the atomic scale, we notice that the contact line position is usually not perfectly *pinned* at one position. It is actually free to adjust its microscopic position depending on external constraints. Contact line *pinning* at a continuous domain boundary should be considered as localization of the contact line within the transition zone between adjacent domains. This finite rigidity of contact line pinning has a second consequence that is arguably even more fundamental: It allows for a competition between pinning and deformation of the drop shape. In our discussion above, we focused completely on the contact line and neglected the fact that competing drop configurations, say, in Figure 1.22, also have different liquid–vapor interfacial areas. This is indeed justified for perfectly sharp domain boundaries. For domain boundaries with a gradual variation of the wettability, however, the stiffness of the boundary competes with the stiffness of the liquid–vapor interface. If the latter is stronger, the metastability disappears and the uniqueness of the equilibrium drop morphology is reestablished. This gives rise to the notion of *strong defects* versus *weak defects* that was introduced in the seminal paper on wetting of heterogeneous surfaces by Joanny and deGennes [12].

The difference between strong and weak defects is easily illustrated by a two-dimensional *drop* of liquid filling the space between a solid block of finite length and a flat solid surface that contains a wetting defect, as sketched in Figure 1.24. The free liquid surface is pinned to the bottom right corner of the block at point $X$. The pressure in the liquid is kept at zero such that the liquid–vapor interface is flat. The contact line position $x_{eq}$ adjusts itself according to the local Young angle on the substrate. At the contact line, the liquid surface tension pulls toward the left (for the situation sketched with $\theta_Y < 90^\circ$) with a force $f_\gamma = \gamma \cos\theta(x) = \tilde{x}/\sqrt{1+\tilde{x}^2}$, where $\tilde{x} = x/H$ is the normalized

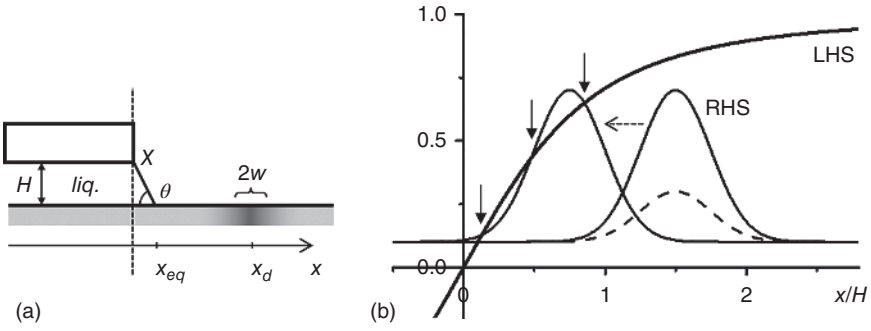


**Figure 1.24** Strong defect versus weak defect. (a) Illustration of geometry with liquid filling the gap between a solid block and the solid surface with a wetting defect at $x = x_d$ with a width $2w$. (b) Force balance at the contact line versus normalized contact line position. Thick solid line: surface tension force according to left-hand side (LHS) of Eq. (1.49). RHS: defect force according to right-hand side of Eq. (1.49) for Gaussian wetting defects of variable strength and position ($\Delta\cos\theta_{1,2} = 0.6$; $\Delta\cos\theta_3 = 0.2$; $\tilde{x}_{d;1,3} = 1.5$; $\tilde{x}_{d;2} = 0.75$; $\tilde{w}_{1,2,3} = 0.25$).

position of the contact line. The solid surface pulls toward the right with a force $f_{surf} = \gamma_{sv}(x) - \gamma_{sl}(x) = \gamma \cos\theta_Y(x)$. The forces are balanced if

$$\frac{\tilde{x}}{\sqrt{1+\tilde{x}^2}} = \cos\theta_Y(\tilde{x}) \tag{1.49}$$

This is an implicit equation for the contact line position $\tilde{x}$ with the obvious solution $\cos\theta(x) = \cos\theta_Y(x)$. Yet, this solution is not always unique. To be specific, we consider a specific wetting defect at $x = x_d$ where the local contact angle is lower than on the rest of the surface. To be specific, we choose a Gaussian variation of the surface energy such that

$$\cos\theta_Y(x) = \cos\theta_Y^{\infty} + \Delta\cos\theta_Y \ \exp(-(x-x_d)^2/2w^2) \tag{1.50}$$

The equilibrium position of the contact line can be obtained most easily by a graphical solution of Eq. (1.49). Figure 1.24b shows the LHS (thick line) and the RHS (thin line) of Eq. (1.49) for a strong and for a weak defect with large and small amplitude, respectively. If the defect is sufficiently far away from the origin, there is only one unique contact line position given by the intersection point of the two curves. If we shift the center of the defect further toward the left, however, there appear at some point three intersection points, as indicated by the arrows in Figure 1.24b. While the middle one is unstable, the two others represent two competing mechanically stable configurations of the contact line. As usual, the existence of such metastable states implies pinning the appearance of a hysteresis loop of the contact line position upon moving the defect from right to left and back. Abrupt depinning events occur whenever the physically realized contact line position becomes unstable, i.e. whenever the corresponding intersection point in Figure 1.24b disappears. Assuming that the contact line position is initially given by the leftmost arrow, this happens if we shift the Gaussian defect a little further toward the left. At some point, the leftmost and the middle intersection points merge into one. Subsequently, this solution disappears. This is

characteristic for a strong defect. For a weak defect such as the one characterized by the dashed defect force in Figure 1.24b, there is always only one single stable solution for the contact line position, for all values of $x_d$. This leads a very clear criterion to distinguish between weak and strong defects: A defect is strong, i.e. stiffer than the liquid–vapor interface, if the maximum slope of the defect force (RHS in Figure 1.24b) exceeds the maximum slope of the surface tension force (LHS). Vice versa, if the slope is lower, the defect is weak. The reader is invited to analyze this problem in more detail (see Problem 1.5). Wetting defects with tunable strength are easy to fabricate using EW. Experiments showed the appearance and disappearance of contact line pinning and trapping of drops [13, 14].

### 1.7.4 Optimum Contact Angle on Heterogeneous Surfaces: The Laws of Wenzel and Cassie

Even if a drop can in general not reach its true equilibrium contact angle on a heterogeneous surface by means of thermal excitation, there is nevertheless a specific contact angle that minimizes the total surface energy, both for rough and for chemically heterogeneous surfaces.

For flat surfaces with variable heterogeneity as shown in Figure 1.22c,d, we can rewrite Eq. (1.46) as

$$G = \gamma \left[ L_{lv} - \int_{x_A}^{x_B} dx \cos \theta_Y[x] \right] \tag{1.51}$$

where the width of the drop $L = x_B - x_A$ and the drop surface arc length $L_{lv}$ are connected by the constraint of constant volume. Figure 1.25 shows a typical result plotted as a function of the macroscopic apparent contact angle $\theta$ for $L \gg l$. The thick vertical arrow indicates the position of the absolute energy minimum. Similarly looking curves can be generated for topographically structured surfaces. While any local minimum in Figure 1.25 is mechanically stable, drops can nevertheless be brought close to the absolute minimum by a suitable, e.g. mechanical or electrical excitation that allows them to cross energetic barriers between adjacent minima. The value of the optimum apparent contact angle can be derived in the same way as in our energy-based derivation of Young's law. Let us consider a surface consisting of a random distribution of lyophilic patches with area fraction

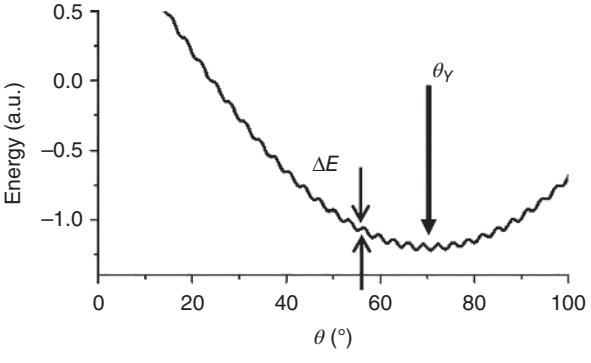


**Figure 1.25** Free energy of a sessile drop on a surface with alternating stripes of high and low contact angle leading to a variety of locally stable drop configurations in the vicinity of the absolute energy minimum.

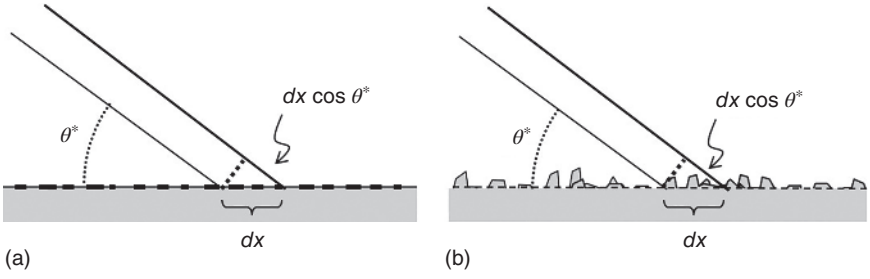


**Figure 1.26** Virtual contact line displacement *dx* and derivation of optimum apparent contact angle $\theta^*$ on chemically heterogeneous (a) and rough (b) surface.

$f_A$ and of lyophobic patches $B$ with an area fraction $f_B = 1 - f_A$ (Figure 1.26a). If we assume that the drop has enough energy to explore all possible configurations and if we assume further that any virtual displacement $dx$ comprises a surface area sufficiently large to represent the average composition of the surface, the variation of the surface energy upon a contact line displacement $dx$ reads

$$\delta E_{surf} = dx\,[f_A(\gamma_{sl}^A - \gamma_{sv}^A) + f_B(\gamma_{sl}^B - \gamma_{sv}^B) + \gamma\cos\theta] \tag{1.52}$$

Equating this expression to zero yields the optimum apparent contact angle $\theta^*$ on the heterogeneous surface with

$$\cos\theta^* = f_A\cos\theta_Y^A + f_B\cos\theta_Y^B \tag{1.53}$$

This expression is known as Cassie's law for the contact angle on heterogeneous surfaces. If the surface becomes homogeneous, i.e. if either $f_A \to 1$ and $f_B \to 0$ or vice versa, we recover Young's contact angle of the corresponding homogeneous surface, as it should be.

An analogue expression for topographically rough surfaces was derived by Wenzel along the same spirit. Wenzel noticed that omnipresent microscopic roughness enhances the actual surface area of the solid as compared with the apparent projected surface area $A$ (Figure 1.26b). To characterize the topographic roughness, he introduced the parameter $r = A_m/A$, which specifies the ratio between the true microscopic surface area $A_m$ and the apparent projected one. As a consequence of this enhancement of the interfacial area, the weight of the contributions of $\gamma_{sl}$ and $\gamma_{sv}$ in the variation of the surface energy increases:

$$\delta E_{surf} = dx(r\cdot(\gamma_{sl} - \gamma_{sv}) + \gamma\cos\theta) \tag{1.54}$$

Equating this expression to zero yields Wenzel's equation for the optimum apparent contact angle on a rough surface:

$$\cos\theta^* = r\,\cos\theta_Y \tag{1.55}$$

Since $r > 1$ by definition, Wenzel's law implies that roughness *drives* the contact angle away from 90°: For $\theta_Y > 90^\circ$, $\theta^*$ becomes even larger than $\theta_Y$ with increasing $r$, and conversely, for $\theta_Y < 90^\circ$, we have $\theta^\star < \theta_Y$. This is exactly what we should expect given the enhanced weight of the drop–substrate interface due to the larger absolute interfacial area.

Note, however, that both derivations are based on the rather strong assumptions that the contact line is able to explore the representative fraction of the surface. This is in contrast to our earlier observation that energy barriers due to surface heterogeneities larger than a few nanometer are much higher than thermal energy. Equations (1.53) and (1.55) thus describe equilibrium states that often cannot be reached in practice. It is therefore not surprising that measurements of contact angles on heterogeneous surfaces frequently deviate from these predictions.

### 1.7.5 Superhydrophobic Surfaces

Wetting of rough hydrophobic surfaces leads to the well-known phenomenon of superhydrophobicity, which has attracted increasing attention since novel micro- and nanofabrication technologies have enabled the production of increasingly complex surface patterns. Superhydrophobicity arises for very rough hydrophobic surfaces. Figure 1.27 shows a generic geometry of simple superhydrophobic surfaces consisting of an array of regularly spaced pillars. According to our discussion of Wenzel's law in the preceding section, roughness increases the contact angle of hydrophobic surfaces because it increases the area of the energetically unfavorable solid–liquid interface. The optimum contact angle $\theta_W^*$ in the so-called Wenzel state, in which liquid fills the cavities of the surface roughness as sketched in Figure 1.27a, is readily calculated by inserting the roughness factor $r$ into Wenzel's equation. For a simple array of pillars with height $h$ and periodicity $\lambda$ as shown in Figure 1.27, we find $r = 1 + 2h/\lambda$.

It turns out, however, that the actual contact angle observed on superhydrophobic surfaces is often substantially higher than predicted by Wenzel's law, Eq. (1.55). The reason is that the drop does not necessarily fill the cavities of the rough surface topography. Provided that the surface is sufficiently rough,

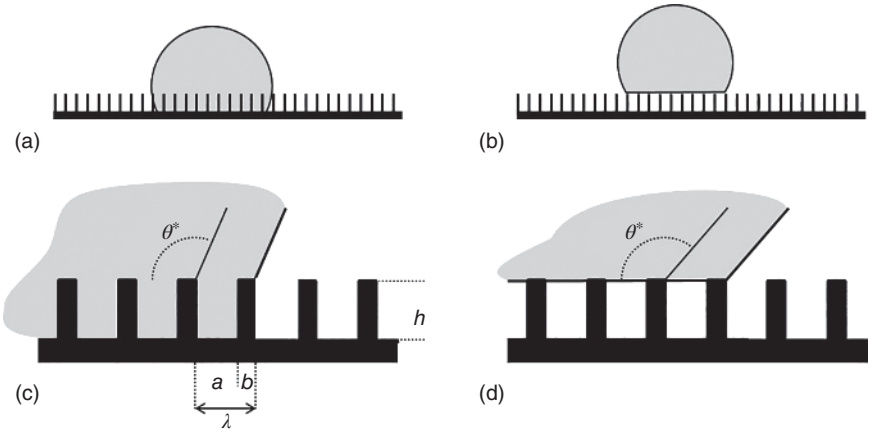


**Figure 1.27** Wetting of rough hydrophobic surface and derivation of optimum contact angle $\theta^*$. (a) Wenzel state with liquid filling the cavities between the pillars. (b) Superhydrophobic Cassie–Baxter state with air entrapped in the cavities. (c,d) Microscopic views near the contact line for Wenzel and Cassie–Baxter state, respectively.

the drop can instead assume a configuration, in which it rests on the tops of the pillars while the space in between remains filled with air, as sketched in Figure 1.27b. This is the superhydrophobic or *Cassie–Baxter* state. It is characterized by a massively reduced solid–liquid interfacial area as compared with a flat surface. This reduction of the solid–liquid interfacial area is the basis of many advantageous properties of the superhydrophobic state, including the very high contact angle $\theta^*$, the very low contact angle hysteresis, the self-cleaning properties, hydrodynamic slip, etc. The drop–substrate interface in the Cassie–Baxter state consists of a series of alternating domains of solid–liquid interface and liquid–vapor interface (see Figure 1.27d). Hence, we can calculate the optimum value of $\theta^*$ using Cassie's equation, Eq. (1.52), using air with a contact angle of 180° as one of the two materials of this *chemically heterogeneous* substrate. If we denote the area fraction of the pillars as $f = b/\lambda$, the corresponding one of air is $1 - f = a/\lambda$. Inserting these ingredients in Eq. (1.53), we find that the optimum contact angle $\theta^*_{CB}$ in the Cassie–Baxter state is determined by

$$\cos\theta^*_{CB} = f(\cos\theta_Y + 1) - 1 \tag{1.56}$$

Here, $\theta_Y$ is Youngs angle on a flat surface made of the material of the pillars. The Cassie–Baxter state is stabilized by the fact that the contact line is pinned at the edges of the pillars, as illustrated in Figure 1.27c,d. $\theta_Y$ obviously needs to be larger than 90° to support a Cassie–Baxter state. Otherwise, the contact line would not remain pinned, and the liquid would be sucked into the cavities by the then negative Laplace pressure. $\theta^*_{CB}$ approaches 180° upon minimizing the area fraction $f$ of the pillars. This is qualitatively plausible: For $f \to 0$, the drop essentially rests on a layer of air – with few pillars in between to support it. Yet, it is also plausible that such a state is not very stable and prone to collapse into the Wenzel state.

It is worthwhile to reiterate an important aspect form our discussion in the preceding section: Drops can assume many locally mechanically stable configurations on superhydrophobic surfaces. The energy barriers between these states are large compared with thermal energies. There is a family of Wenzel-like morphologies covering a variable number of pillars, and likewise, there is a family of Cassie–Baxter-like morphologies covering a variable number of pillars. Depending on the surface geometry, even mixed configurations with partially liquid-filled and partially air-filled cavities can be stable. The configurations with the optimum contact angles $\theta^*_W$ and $\theta^*_{CB}$, respectively, are thus the states that minimize to total surface energy in the spirit of Figure 1.25. Because the solid–liquid interfacial area is very small in the superhydrophobic Cassie–Baxter state, it turns out that the energy barriers are also rather low, and hence the practically realized contact angles are close to $\theta^*_{CB}$. This is also reflected in the low contact angle hysteresis in the superhydrophobic state. The barrier between the Cassie–Baxter-like and the Wenzel-like morphologies is often very high. The morphology of the drop thus always depends on the history, e.g. the manner of depositing the drop on the surface. In that sense, the expression *superhydrophobic surface* is misleading. Superhydrophobicity characterizes a specific state of wetting of a drop on a rough hydrophobic surface

rather than an intrinsic property of the surface. Almost all surfaces denoted as *superhydrophobic* support drops both in the superhydrophobic Cassie–Baxter state and in the Wenzel state.

Figure 1.28a illustrates the transition of a drop from the Cassie–Baxter state to the Wenzel state upon evaporation. While the drop volume gradually decreases without noticeable variation of the contact angle in the top row of images, a sudden dramatic reduction of the contact angle takes place between the first two images of the second row (see arrow). This reduction of the contact angle is caused by sudden transition from the Cassie–Baxter state to the Wenzel state: The Cassie–Baxter morphology became unstable due to the reduction of the drop size. To understand the origin of this transition, we note first that the pressure inside the drop has to be constant in mechanical equilibrium. (We assume that the drop is small compared with the capillary length.) Hence, Laplace's law tells us that the curvature $\kappa = 1/R$ of all the liquid micromenisci spanning the gaps between adjacent pillars at the drop–substrate interface has to be the same as the macroscopic curvature of the drop. The latter increases as the radius of the drop decreases during the evaporation. As a consequence, the micromenisci bend and deflect more and more as the drop shrinks. From our discussion of Gibbs pinning criterion, we can immediately identify a limit of this process: If the deflection $\Delta h$ of the menisci becomes too large, the angle $\alpha$ in Figure 1.28b exceeds the contact angle on the vertical sidewall of the pillar. As a consequence, the contact line is no longer pinned, and the liquid invades the cavity: The drop undergoes a transition to the Wenzel state. Evaluating elementary geometric relations, we find that the critical drop radius $R_c$ at the transition is given by $R_c = -a/2 \cos\theta_Y$. Since $\cos\theta_Y \approx -0.5$ for typical hydrophobic materials, contact line depinning only takes place when $R_c$ has decreased to a value of the order of the pillar spacing. Note, however, that this scenario only takes place if the pillars are not too sparsely spaced on the surface. If the aspect ratio $h/\lambda$ is very low, as it is desirable to maximize $\theta^*_{CB}$, contact line depinning is preceded by the micromenisci touching the bottom of the cavity, i.e. when the deflection $\Delta h$ reaches the height of the pillars,

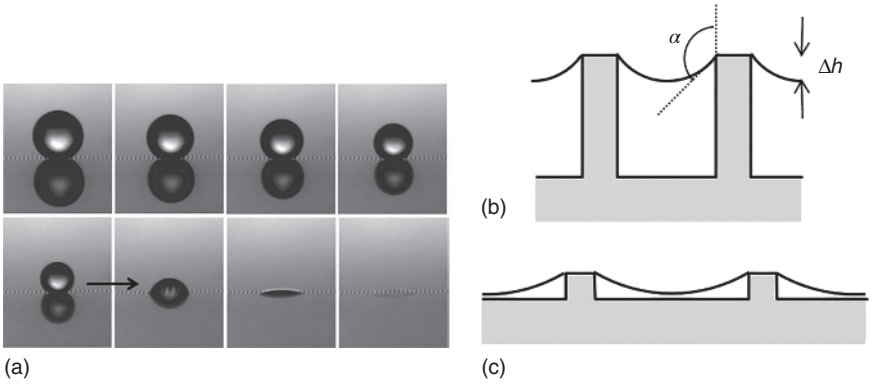


**Figure 1.28** Cassie-to-Wenzel transition on superhydrophobic surfaces. (a) Video snapshots. Source: Reproduced with permission from [15]. (b) Stability limit for surface pattern with large aspect ratio. (c) For low aspect ratio.

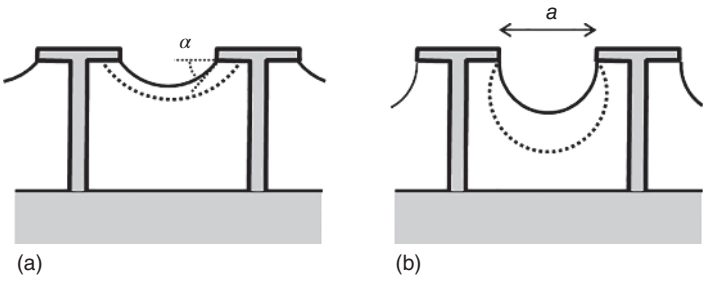


**Figure 1.29** Stability limits of structured surfaces with overhangs leading to superoleophobic behavior. (a) Depinning according to Gibbs criterion. (b) Destabilization due to negative pressure gradient criterion.

as sketched in Figure 1.28c. Geometric considerations show that the critical drop radius in this case is given by $R_c = a^2/8h$ for $a \ll R$.

In the examples given above, the Cassie–Baxter configuration is destabilized because the decreasing drop volume increases the pressure. In other situations, the pressure in the liquid phase may be controlled by some parameters such as the hydrostatic pressure for superhydrophobic surfaces completely submerged under water or the impact speed for drops impinging onto a superhydrophobic surface. In all cases, the stability of superhydrophobic surfaces can be enhanced by decreasing the spacing between the pillars. Since the width of the pillars has to be scaled down simultaneously to maintain a high contact angle, superhydrophobic surfaces that combine high contact angles and good stability against pressure typically require surface patterns on the nanometer scale. Particularly stable surfaces can be achieved by creating surface patterns with overhangs, as shown in Figure 1.29. A surface with overhangs can sustain a Cassie–Baxter state – meaning a state with entrapped air underneath the drop – even if the liquid displays a contact angle $\theta_Y < 90^\circ$. As long as the pressure is not too high, the angle $\alpha$ in Figure 1.29a remains smaller than $\theta_Y$, and the contact line remains pinned at the bottom edge of the overhang. This principle allows to design not only superhydrophobic but also superoleophobic surfaces, i.e. surfaces that display a very large contact angle and very low hysteresis for low surface tension liquids. Upon exposure to liquid at enhanced pressure, these surfaces display another instability mechanism in addition to the ones explained above: By geometry the radius of curvature of the meniscus in Figure 1.29 is $r = a/2 \sin\alpha$, and the corresponding pressure drop across the interface is $\Delta p = \gamma/r$. $\Delta p$ has a maximum for $\alpha = 90^\circ$, where $r = a/2$, as sketched in Figure 1.29b. For larger deflections of the meniscus, $d\Delta p/dV$ becomes negative. In this case, the Cassie–Baxter state becomes unstable, and the meniscus spontaneously expands and displaces the air in the cavities of the superhydrophobic surface.

### 1.7.6 Wetting of Heterogeneous Surfaces in Three Dimensions

Our considerations so far were limited to two-dimensional systems. While illustrating many important aspects, wetting of heterogeneous surfaces in three dimensions involves one important additional aspect: Any local displacement

of the contact line entails a distortion of the adjacent free liquid surface. Such deformations give rise to an additional interfacial area and thus an excess energy. This results in a wavevector-dependent stiffness of the interface that tends to restore the average shape of the surface away from the contact line.

We will limit our discussion to the case of small deformations, for which we can calculate the response of the liquid surface and hence its stiffness analytically. We consider the specific problem a liquid surface parameterized by some function $h(x, y)$. On average, we assume that the surface is flat with $h \equiv h_0$. Let us now introduce a periodic distortion of the surface in one direction, i.e. we impose a constraint $h(x = 0, y) = h_0 + \Delta h \cos qy$ with a wavevector $q = 2\pi/\lambda$. Such as situation can arise, for instance, if a plate with a suitable wettability pattern is immersed into a liquid bath, as sketched in Figure 1.30. (Note that we do not specify the actual wettability pattern; we simply assume that there is a wettability pattern that ensures a sinusoidal variation of the contact line. From the previous discussions, it should be plausible that this is enough to calculate the response of the liquid surface.)

The question is how the amplitude of the corrugation decays as a function of the distance from the $(y, z)$ plain. With these specifications, the problem is actually rather simple: All we need to do is solve the Young–Laplace equation with the specific boundary conditions that the surface follows the imposed perturbation at $x = 0$ and that it is flat for $x \to \infty$. The latter implies $\Delta P_L = \gamma\kappa = 0$. If we also assume that the amplitude of the imposed perturbation is small, i.e. $\Delta h\, q \ll 1$, we simply need to solve the homogeneous Laplace equation $\nabla^2 h(x, y) = 0$. Using separation of variables, i.e. writing $h(x, y) = f(x)g(y)$, the reader can quickly find the solution for the surface profile:

$$h(x, y) = \Delta h \cos qy\, e^{-qx} \tag{1.57}$$

Hence, we find that the amplitude of the corrugation decays exponentially with increasing distance from the imposed perturbation with a decay constant that is given by the wavevector $q$ of the perturbation. Perturbations with a high spatial

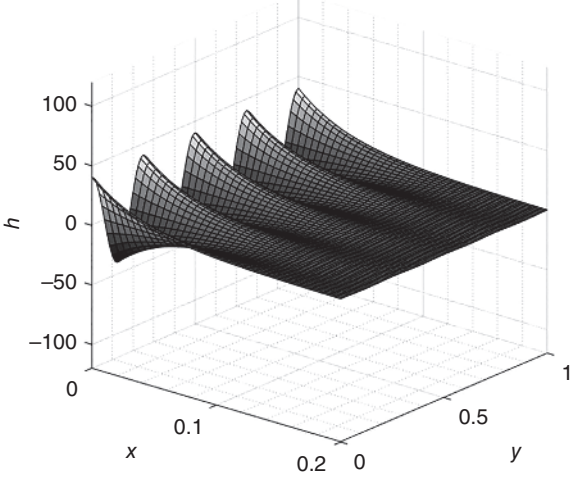


**Figure 1.30** Decay of a modulation imposed on a liquid surface.

frequency thus decay quickly, and vice versa, long wavelength perturbations affect the surface profile over longer distances. We obtained this result here in a linearized model. The linearization implies that the superposition principle applies. To the extent that the amplitude is sufficiently small, we can thus calculate the deformation of the surface for arbitrary imposed perturbations. As usual, many qualitative aspects of the linearized model survive for larger perturbations.

Knowing the full solution of the surface profile, it is easy to show that the resulting excess surface energy scales as $\gamma q\ \Delta h^2$, corresponding to a surface with an effective stiffness $k(q) = \gamma q/2$; see Problem 1.6.

### 1.7.7 Wetting of Complex Surfaces in Three Dimensions: Morphology Transitions, Instabilities, and Symmetry Breaking

The discrete transitions between competing wetting morphologies discussed in the context of Figures 1.22 and 1.23 and for the superhydrophobic surfaces in Figures 1.28 and 1.29 were somewhat simplified because we limited ourselves to two-dimensional problems. Neglecting gravity, this implied that any section of a free liquid surface had the shape of a circular arc in order to guarantee a constant pressure within the fluid. In three dimensions, the constant mean curvature requirement expressed in the Young–Laplace equation allows for a much broader class of liquid morphologies. As already discussed the resulting surface shapes can be quite complex and at times counterintuitive to predict, in particular in the presence of complex boundary conditions imposed by structured solid surfaces. For instance, one of the goals of the experiments shown in Figure 1.4b was to explore the use of surfaces with wettability patterns to control the flow of fluids for microfluidic applications in an open configuration without restrictive solid channel walls. However, as the fluid volume on the hydrophilic ducts was increased, the initial fluid configuration consisting of sections of cylinders with a translationally invariant cross section became unstable, and thick localized *bulges* of liquid appeared. While perhaps disappointing from an applied perspective, it turns out that this kind of spontaneous transition between different types of liquid morphologies with a different symmetry is an important intrinsic characteristic that needs to be taken into account whenever designing fluidic devices involving free liquid surfaces. Such transitions can occur upon variations of many different control parameters, including the liquid volume, pressure, the geometry, and – in particular for EW – the contact angle. In view of the freedom of the liquid surface to adjust its shape in three dimensions, a quantitative analysis of the possible equilibrium configurations and the transitions among them generally requires a detailed numerical analysis.

Figure 1.31a shows the result of a numerical minimization of the surface energy of a drop of liquid of fixed volume deposited onto a lyophilic patch (see top figure) with $\theta_Y = 10^\circ$. Most of the liquid accumulates in an elongated drop on the wide section of the patch with a rather small curvature. Only a small fraction of the fluid wets the narrower horizontal lyophilic stripe. For the same liquid volume but a slightly larger contact angle of $30^\circ$ on the patch, the narrow section remains

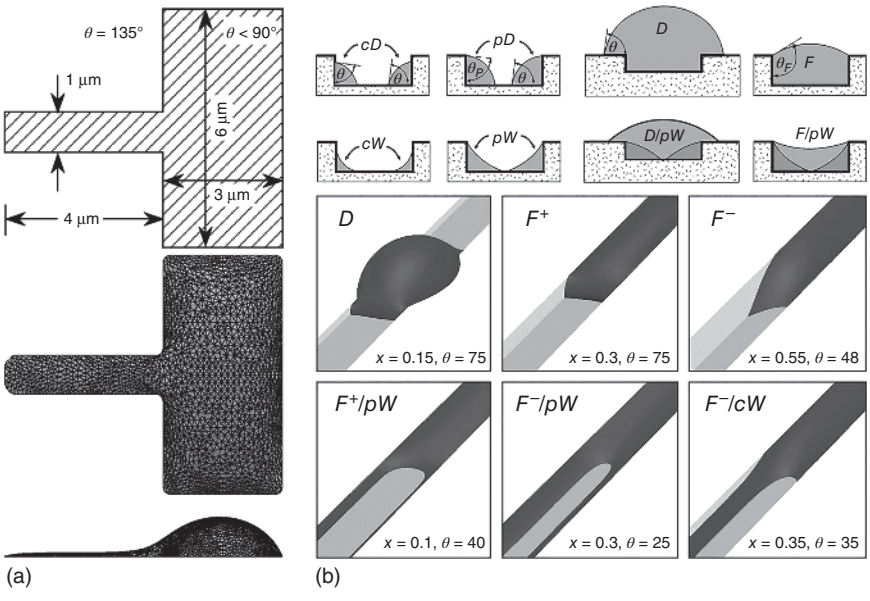


**Figure 1.31** Examples of wetting morphologies on structured surfaces. (a) Calculated wetting morphology of a drop on a rotated-T-shaped lyophilic patch (top panel) on a hydrophobic surface. Middle and lower panels: top view and side view of the equilibrated fluid shape. Source: Darhuber et al. 2000 [16]. Adapted with permission of AIP Publishing. (b) Competing wetting morphologies on a surface with a rectangular groove of variable aspect ratio and contact angle. Top panels: cross-sectional views; bottom panels: 3D views of a series of morphologies. Source: Seemann et al. 2005 [17]. Adapted with permission of PNAS.

completely bare of fluid. Figure 1.31b shows a series of liquid configurations for a drop deposited onto a solid surface with a rectangular groove. Depending on the contact angle and on the aspect ratio $X$ of the groove, an amazing variety of liquid morphologies appears, including localized drops, drops in coexistence with liquid filaments that can have positive or negative curvature with their edges being pinned or not being pinned to the upper corner of the groove. These examples illustrate the richness of possible morphologies encountered upon wetting structured surfaces.

Despite the richness there are a couple of generic phenomena that are frequently observed in the context of morphology transitions in complex geometries. One of them is spontaneous symmetry breaking at a morphology transition. Figure 1.32a,b shows two examples, a pair of two communicating liquid menisci and a drop confined between a flat surface and a sphere. The first example can either be considered as a two-dimensional system with liquid confined between two parallel solid surfaces or as a cross section through a short cylindrically symmetric tube with a spherical cap-shaped meniscus on each side. In both cases, the liquid assumes a mirror-symmetric configuration with two menisci of equal radius if the liquid volume is below a certain critical volume $V_c$. For larger volumes, the liquid assumes an asymmetric configuration as shown in the right panel of Figure 1.32a. In this case, the two menisci are complementary spherical caps

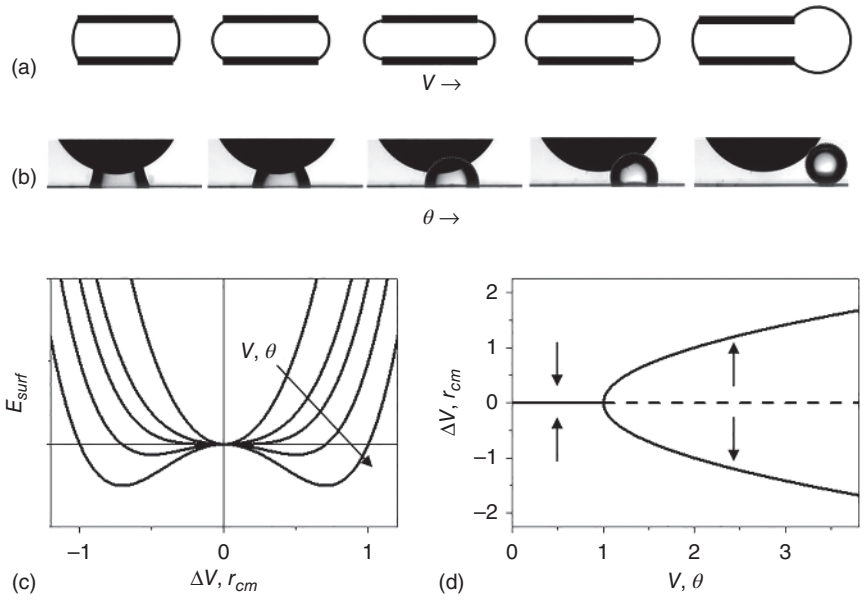


**Figure 1.32** (a) Schematic illustration of spontaneous symmetry breaking of communicating drops upon increasing the liquid volume $V$ along the arrow. (b) Snapshots of symmetry-breaking expulsion of a drop confined between a sphere and a flat surface upon increasing the contact angle from $\theta < 90^{\circ}$ to $\theta > 90^{\circ}$. Source: Experimental data taken from de Ruiter et al. [18]. (c) Schematic of the energy landscape for the morphology transitions in (a) and (b). Control parameters $V$ or $\theta$ increase along the arrow. (d) Pitchfork diagram of the equilibrium value of the asymmetry parameter versus the control parameter. The critical value of $V_c$ and $\theta_c$ was set to 1. Solid lines, stable solutions; dashed line, unstable solution branch; arrows indicate direction of evolution toward equilibrium upon perturbation.

of one sphere (or circle) to ensure that the Laplace pressure is the same on both sides. The stability of this configuration can be assessed in the same manner as our analysis of the Rayleigh–Plateau instability of a liquid jet; see Figure 1.5. The symmetric configuration is stable as long as the transfer of a small volume of liquid $\delta V$ from the left meniscus to the right generates a pressure difference between the two menisci that counteracts the perturbation. This analysis, which the reader is invited to carry out in Problem 1.7, shows that $V_c$ corresponds to the volume for which the radius of the two protruding menisci equals the radius of the tube (or half the distance between the plates). The nature of the symmetry-breaking instability is closely related to the maximum drop pressure criterion controlling the collapse of reentrant superhydrophobic surfaces discussed in Figure 1.29b.

Mathematically, symmetry-breaking morphology transitions can be described in the language of bifurcations of dynamic systems theory. In the vicinity of the critical volume, we can expand the surface energy of the system in even powers of an asymmetry parameter $\Delta V = V_{left} - V_{right}$:

$$E_{surf}(\Delta V) = \alpha (V_c - V) \Delta V^2 + \beta \Delta V^4 \tag{1.58}$$

where $\alpha$ and $\beta$ are positive coefficients. For $V < V_c$ the prefactor in front of the quadratic term is positive. As a consequence, $E_{surf}$ has a unique minimum at

$\Delta V = 0$ as shown in Figure 1.32c,d. As $V$ is increased beyond $V_c$, the prefactor in front of the quadratic term changes sign, and hence the energy landscape assumes a double-well character with two equivalent minima at symmetric values:

$$\Delta V_{eq} = \pm\sqrt{\alpha(V - V_c)/2\beta} \tag{1.59}$$

(Physicists will notice the analogy of this description with Landau's mean field theory of second-order phase transitions in thermodynamics.) If the system is driven into the symmetry-broken state by increasing the control parameter beyond its critical value, it spontaneously chooses one of the two in principal equivalent local minima. Upon increasing the control parameter further, the absolute value of the asymmetry parameter increases further in a continuous manner as specified in Eq. (1.59).

The same type of analysis applies to a large variety of morphology transitions involving symmetries. The drop confined between a sphere and a plate shown in Figure 1.32b is such an example, where the contact angle rather than the drop volume is the control parameter and the radial coordinate $r_{cm}$ of the center of mass of the drop is the asymmetry parameter. The drop is in a cylindrically symmetric state at $r_{cm} = 0$ if the contact angle is below a certain critical angle $\theta_c$. Upon increasing $\theta$ beyond $\theta_c$, e.g. by means of EW [18], the symmetry is spontaneously broken, and the drop moves away from the symmetry axis in a continuous manner analogue to Eq. (1.59). In this case, breaking the symmetry involves the spontaneous selection of an arbitrary azimuthal angle out of a continuum of possible states.

For the cases discussed above, the asymmetry parameter evolves continuously and reversibly as a function of the control parameter. This is different from the morphology transitions discussed earlier that involved an abrupt depinning of contact lines from pinning sites (Figures 1.22, 1.23, and 1.29) and thus abrupt and irreversible variations of the drop shape beyond a critical of some control parameter. The latter transitions are discontinuous. General criteria for the occurrence of continuous versus discontinuous transitions are described on an abstract level in mathematical textbooks on bifurcation theory [19].

An important example that introduces additional aspects to the phenomenology of morphology transitions is the wetting of curved solid surfaces such as fibers. The finite curvature of the fibers introduces the peculiar phenomenon that any coating film of constant thickness is intrinsically unstable even if the liquid completely wets the fiber. This aspect causes important practical challenges in coating technology, e.g. for textile fibers and for insulating coatings on electrical wires. Physically, the origin of this instability is perfectly plausible. If we review our discussion of the Rayleigh–Plateau instability of liquid jets (see Figure 1.5), we can see that the exact same analysis of the underlying linear instability applies to thin liquid layers on a fiber as well as long as the amplitude of the perturbation does not exceed the film thickness. As a consequence, even for $\theta_Y = 0$, the liquid is localized in a drop on the fiber. Qualitatively, there are two different morphologies for wetting a fiber, a cylindrically symmetric *barrel* morphology and a symmetry-broken *clamshell* morphology, in which the drop is attached to the side of the fiber, as can be observed, e.g. for dew drops on spider webs (see Figure 1.33). There are two control parameters governing the wetting of such structures, the

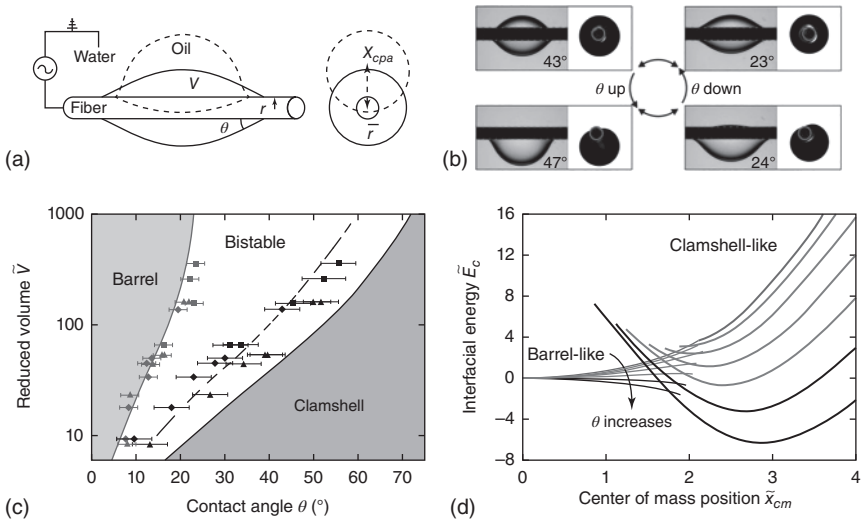


**Figure 1.33** Fiber wetting. (a) Cylindrically symmetric, topologically multiply connected barrel morphology (solid) versus symmetry-broken singly connected clamshell morphology (dashed). (b) Experimental snapshots of competing morphologies including hysteresis upon varying $\theta$. (c) Morphology diagram indicating the ranges of stability of the competing morphologies. Solid lines, numerical stability limits; dashed, equal absolute energy of both barrel and clamshell morphology. Symbols, experimental data. (d) Numerically calculated energy landscape of barrel-like and clamshell-like morphologies versus radial position of center of mass of the fluid for variable contact angle. Source: Eral et al. 2011 [20]. Reproduced with permission of Royal Society of Chemistry.

contact angle $\theta_Y$ on the fiber and the ratio between the drop size and the fiber radius $r$. For the latter, it is convenient to think in terms of the dimensionless drop volume $V/r^3$. For certain values of the parameters, the limiting wetting behavior is easy to determine: For $\theta \to 0$, the system will try to maximize the fiber–drop interfacial area, thus favoring the barrel state. Similarly, the clamshell state will be preferred for high contact angles. Furthermore, it is clear that the clamshell state is preferred for $\tilde{V} = V/r^3 \to 0$ because the curvature of the fiber becomes negligible in this limit on the scale of the drop (see Figure 1.33c). Away from these limits, the competition between the two morphologies is more complex. Clamshells are essentially somewhat distorted sessile drops with a single three-phase contact line. The barrel morphology is qualitatively different. The solid fiber effectively pierces a hole through the liquid, giving rise to two separate contact lines at each end. Topologically speaking, a clamshell drop is simply connected, whereas a barrel drop is not. As a consequence of this fundamental topological distinction between the two competing morphologies, a simple continuous evolution from the symmetrical to the symmetry-broken morphology is not possible. Instead, there is a wide region in the morphology diagram for which both morphologies are mechanically stable. This gives rise to a pronounced hysteresis if, for instance, the contact angle of a drop of fixed volume is decreased from a large to a small value and subsequently increased again, as illustrated in Figure 1.33b. Correspondingly, the energy diagram as a function of

the asymmetry parameter, illustrated in Figure 1.33d, looks qualitatively different from Figure 1.32c. While the barrel morphology undergoes a linear instability as the contact angle exceeds a certain critical value similar to the symmetric state in the examples given above, its energy curve is intercepted by the energy curve of the clamshell state, which has a minimum at some finite contact angle-dependent radial coordinate. As a consequence, the center of mass of the drop undergoes an abrupt and discontinuous transition to the clamshell state. In the opposite direction, the clamshell state becomes unstable when the drop starts to engulf the fiber at decreasing contact angle. At some point, two opposing sections of the contact line merge on the opposite side from the drop (see bottom right snapshot in Figure 1.33b) to induce the abrupt transition to the barrel state.

From a practical perspective, the discontinuity of this type of morphology transitions involves energy dissipation upon switching, which may be undesirable in certain applications. On the other hand, bistability may be attractive in applications that require digital switching between two discrete states of the system with very distinct properties. Depending on the requirements of a specific application, clever engineering will allow the reader to identify suitable combinations of surface geometries and wettabilities to develop systems with more analogue or more digital response characteristics.

## 1.A Mechanical Equilibrium and Stress Tensor

To analyze force balance in continuum mechanics, it is frequently useful to consider certain control volumes and all the forces acting on them, as we discussed in Section 1.4 in the context of drops under the influence of gravity. In this appendix, we take a step back and consider first a small control volume $dV = dx\,dy\,dz$ around a point $(x_0, y_0, z_0)$ in the absence of gravity. $dV$ is bounded by six surface elements $d\vec{S}_j = dS\,\vec{n}_j$ with normal vectors $\vec{n}_j$. Each surface element experiences forces due to the stresses $T_{ij}$ within the fluid (Figure 1.A.1). The stress tensor $T_{ij}$ indicates the stress in the coordinate direction $\vec{e}_i$ acting on a surface element with the surface normal along $\vec{e}_j$. The total force acting on $dV$ is therefore

$$dF_i = \sum_k T_{ik} dS_k \tag{A.1}$$

In mechanical equilibrium the stress tensor is isotropic, because finite shear stresses would generate fluid motion. Hence, we know that $T_{ij} = \delta_{ij} T_{ij}$, where $\delta_{ij}$ is the Kronecker delta symbol. Equation (A.1) then reduces to

$$\begin{aligned} dF_i &= \left[ T_{ix}\left(x_0 - \frac{dx}{2}\right) - T_{ix}\left(x_0 + \frac{dx}{2}\right) \right] dS\,\vec{e}_x \\ &\quad + \left[ T_{iy}\left(y_0 - \frac{dy}{2}\right) - T_{iy}\left(y_0 + \frac{dy}{2}\right) \right] dS\,\vec{e}_y \\ &\quad + \left[ T_{iz}\left(z_0 - \frac{dz}{2}\right) - T_{iz}\left(z_0 + \frac{dz}{2}\right) \right] dS\,\vec{e}_z \\ &= -\partial_x T_{ix} dx\,dydz\,\vec{e}_x - \partial_y T_{iy} dy\,dxdz\,\vec{e}_y - \partial_z T_{iz} dz\,dxdy\,\vec{e}_z = 0 \end{aligned} \tag{A.2}$$

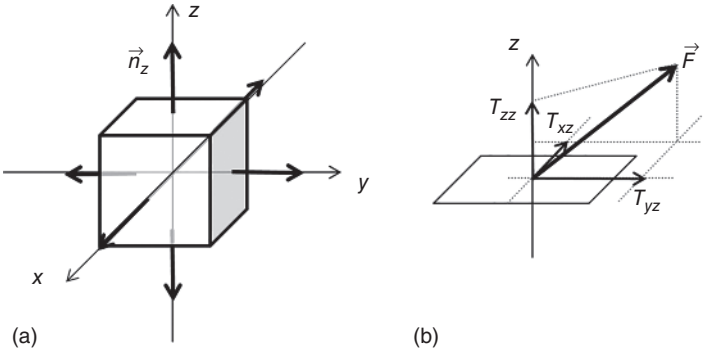


**Figure 1.A.1** (a) Illustration of a control volume within a fluid. (b) Decomposition of a force acting on the top facet of the control volume into components of the stress tensor.

This implies that $\partial_x T_{ix} = \partial_y T_{iy} = \partial_z T_{iz} = 0$. That is, $T_{ij}$ is constant in space. Because all spatial directions are equal, symmetry reasons allow us to conclude that all three diagonal components are equal. (If the stress in one direction would be larger than in another one, the volume element $dV$ would deform and stretch along the direction(s) of lower pressure, which would contradict our assumption of mechanical equilibrium.) The common value is denoted as the (isotropic) hydrostatic pressure $p = T_{xx} = T_{yy} = T_{zz}$. That is, we can write the stress tensor as $T_{ij} = p\,\delta_{ij}$. In this manner, the Laplace pressure caused by the *directional* surface tension forces at a liquid surface translates into an *isotropic* hydrostatic pressure $p_0 = \Delta P_L$.

In the presence of gravity, the liquid inside the control volume experience the body force $d\vec{f}_g = -\rho g dV\,\vec{e}_z$. Making use of Eq. (A.2), the force balance of all forces acting on $dV$ is then given by

$$\begin{aligned} d\vec{F} &= -\nabla p + d\vec{f}_g = 0 \\ &= -\partial_x p dx\, dydz\,\vec{e}_x - \partial_y p dy\, dxdz\,\vec{e}_y - (\partial_z p dz\, dxdy - \rho g dV)\,\vec{e}_z \end{aligned} \tag{A.3}$$

This implies $\partial_x p = \partial_y p = 0$ and $\partial_z p = \rho g$. Because of the isotropy of the pressure, we find a hydrostatic pressure

$$p = p_0 - \rho g z \tag{A.4}$$

where $p_0$ is again a suitably chosen reference pressure. Again, the directional gravitational body force translates into an *isotropic* pressure acting equally in all directions within the fluid.

## Problems

**1.1** Young's angle minimizes the surface energy of a spherical cap. For spherical caps, the values of $A_{sl}$ and $A_{lv}$ as well as the drop volume $V$ are known geometrical functions of $R$ and $\theta_Y$ (see Table 1.2). Hence we can rewrite Eq. (1.14) as $E_{surf}(R, \theta) = A_{lv}(R, \theta)\gamma + A_{sl}(R, \theta)(\gamma_{sl} - \gamma_{sv})$. (a) Rewrite this

equation as a function of $\theta$ alone using volume conservation and plot $E_{surf}(\theta)$. (b) Show that the angle $\theta^*$ that minimizes $E_{surf}(\theta)$ is given by $\cos\theta^* = (\gamma_{sv} - \gamma_{sl})/\gamma$, i.e. $\theta^* = \theta_Y$.

**1.2** Coffee mug. Consider the shape of a meniscus wetting a vertically immersed solid surface. An example from daily life would be the profile of the liquid surface in our coffee mugs. The coffee has a contact angle $\theta_Y$ on the wall of the coffee mug, which will be close to zero. In the center of the mug, the surface of the coffee is flat. Describe qualitatively the shape of the coffee surface upon approaching the wall. At which distance from the surface do you expect noticeable deformations of the surface? How high will the contact line rise above the flat reference level in the middle of the mug?

**1.3** Force balance on a sessile drop. Consider a sessile drop in two dimensions, i.e. a segment of a circle, with contact angle $\theta_Y$ and height $h$ in the absence of gravity. Show that the sum of all external forces on the right half of the drop vanishes.

**1.4** Capillary rise. Derive Jurin's law, Eq. (1.26), by minimizing the total energy of the system, i.e. surface plus gravitational energy.

**1.5** Strong versus weak wetting defects. Consider a Gaussian wetting defect of variable strength similar to the one sketched in Figure 1.24 with a wettability profile as given in Eq. (1.50) with $\theta_Y^\infty = 120^\circ$, $\Delta\cos\theta_Y = 1$, and $\tilde{w} = 0.025$. (a) Draw a graphical representation of the force balance equation analogue to Eq. (1.50). Is this defect strong or weak? (b) If applicable, draw the force balance curves for all the defect positions corresponding to depinning transitions. (c) Write a computer program to track numerically the position of the contact line upon varying the defect position from $\tilde{x}_d = 2$ to $-2$ and back.

**1.6** Restoration of a perturbed liquid surface. (a) Consider a liquid surface with an imposed surface perturbation as shown in Figure 1.30. Show that the restoring force of the free surface can be interpreted as a harmonic spring with a wavevector-dependent spring constant $k_{eff} = \gamma q/2$. (b) Assume that the imposed contact line position is given by a superposition of sine functions approximating a square wave. Use the first five Fourier coefficients of the harmonic expansion with a global amplitude factor 0.1. Calculate and plot $h(x, y)$ for $y = 0,\ 1/2q, 1/q, 2/q$. Discuss the relation between the surface shape and $k_{eff}(q)$.

**1.7** Instability of two communicating liquid menisci. (a) Consider the geometric configuration shown in Figure 1.32a with two menisci connected by a slit pore. Assume that the system is two-dimensional. Show that the equilibrium configuration of the liquid is symmetric liquid volumes $V$ below a critical liquid volume $V_c$ and that it is unstable for $V > V_c$. If $L$ is the length of the

slit pore and $2a$ the spacing between the solid walls, show that $V_c = 2aL + \pi a^2$. (b) Discuss possible analogies between this symmetry-breaking morphology transition and the bulging transition shown in Figure 1.4b. Source: The reader may want to consult Lenz and Lipowsky [21] for inspiration.

**1.8** Wetting of wedges in two dimensions. (a) Determine the equilibrium shape and position of a drop in a wedge with an opening angle $\alpha$ and a contact angle $\theta_Y$ on the solid walls. Calculate in particular the forces between the drop and the solid surfaces in the tangential and normal direction.

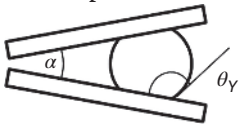


Source: See also Baratian et al. [22] for inspiration.

**1.9** Wetting in a sphere–plate geometry. (a) Argue that the equilibrium shape and radial position $r_c$ of a drop confined between a sphere of radius $R$ and a plate at distance $s$ are given by a truncated sphere at a position $r_c$ displaying Young's angle $\theta_Y$ on both surfaces. (b) Show that $\tilde{r}_c = \sqrt{\tilde{r}^2 \sin^2\theta_Y - (2+\tilde{s})(2\tilde{r}\cos\theta_Y + \tilde{s})}$, where all length scales are given in units of $R$. $\tilde{r}$ is the position-dependent radius of the drop. (c) Show particular the critical contact angle $\theta_c$ below which $\tilde{r}_c(\theta) \equiv 0$ coincides with the onset of an attractive capillary force between the plate and the sphere.

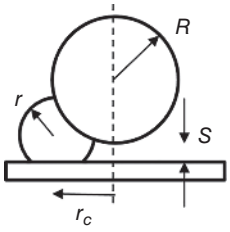


Source: See also de Ruiter et al. [18].

## References

1 deGennes, P. G., Brochard-Wyart, F., and Quéré, D. (2004). *Capillarity and Wetting Phenomena*. New York: Springer.
2 Butt, H. J. and Kappl, M. (2010). *Surface and Interfacial Forces*. Wiley VCH Verlag GmbH & Co. KGaA.
3 Israelachvili, J. N. (1992). *Intermolecular and Surface Forces*, 2e. London: Academic Press.
4 Rowlinson, J. S. and Widom, B. (1982). *Molecular Theory of Capillarity*. Oxford: Clarendon.
5 Gau, H. (1998). Stabilität und Dynamik fluider Mikrostrukturen. PhD thesis. University of Potsdam, Germany.

6 Gau, H., Herminghaus, S., Lenz, P., and Lipowsky, R. (1999). Liquid morphologies on structured surfaces: from microchannels to microchips. *Science* 283: 46–49.

7 Hagedorn, J. G., Martys, N. S., and Douglas, J. F. (2004). Breakup of a fluid thread in a confined geometry: droplet-plug transition, perturbation sensitivity, and kinetic stabilization with confinement. *Phys. Rev. E* 69 (5): 18.

8 Lamb, H. (1932). *Hydrodynamics*. New York: Dover Publications.

9 Pericet-Camara, R., Best, A., Butt, H. J., and Bonaccurso, E. (2008). Effect of capillary pressure and surface tension on the deformation of elastic surfaces by sessile liquid microdrops: an experimental investigation. *Langmuir* 24 (19): 10565–10568.

10 Johnson, R. E. and Dettre, R. H. (1964). Contact angle hysteresis: III: study of an idealized heterogeneous surface. *J. Phys. Chem.* 68: 1744–1750.

11 Oliver, J. F., Huh, C., and Mason, S. G. (1977). Resistance to spreading liquids by sharp edges. *J. Colloid Interface Sci.* 59: 568–581.

12 Joanny, J. F. and de Gennes, P. G. (1984). A model for contact angle hysteresis. *J. Chem. Phys.* 81: 552–562.

13 ‘t Mannetje, D. J. C. M., Banpurkar, A. G., Koppelman, H. et al. (2013). Electrically tunable wetting defects characterized by a simple capillary force sensor. *Langmuir* 29 (31): 9944–9949.

14 ‘t Mannetje, D. J. C. M., Ghosh, S., Lagraauw, R. et al. (2014). Trapping of drops by wetting defects. *Nat. Commun.* 5: 3559.

15 Reyssat, M., Yeomans, J. M., and Quere, D. (2008). Impalement of fakir drops. *Europhys. Lett.* 81 (2): 26006.

16 Darhuber, A. A., Troian, S. M., Miller, S. M., and Wagner, S. (2000). Morphology of liquid microstructures on chemically patterned surfaces. *J. Appl. Phys.* 87 (11): 7768–7775.

17 Seemann, R., Brinkmann, M., Kramer, E. J. et al. (2005). Wetting morphologies at microstructured surfaces. *Proc. Natl. Acad. Sci. U.S.A.* 102 (6): 1848–1852.

18 de Ruiter, R., Semprebon, C., van Gorcum, M. et al. (2015). Stability limits of capillary bridges: how contact angle hysteresis affects morphology transitions of liquid microstructures. *Phys. Rev. Lett.* 114 (23): 234501.

19 Strogatz, S. H. (1994). *Nonlinear Dynamics and Chaos: with Applications to Physics, Biology, Chemistry and Engineering*. Boulder, CO: Westview Press.

20 Eral, H. B., de Ruiter, J., de Ruiter, R. et al. (2011). Drops on functional fibers: from barrels to clamshells and back. *Soft Matter* 7 (11): 5138–5143.

21 Lenz, P. and Lipowsky, R. (1998). Morphological transitions of wetting layers on structured surfaces. *Phys. Rev. Lett.* 80: 1920.

22 Baratian, D., Cavalli, A., van den Ende, D., and Mugele, F. (2015). On the shape of a droplet in a wedge: new insight from electrowetting. *Soft Matter* 11: 7717.